Master's thesis

NTNU
Norwegian University of Science and Technology
Faculty of Information Technology and Electrical Engineering
Department of Engineering Cybernetics

Frida Xiang Nordås Årsandøy

Power optimisation of autonomous rotorcraft

Master's thesis in Industrial Cybernetics
Supervisor: Morten Dinhoff Pedersen
Co-supervisor: Finn Matras
June 2023

NTNU
Norwegian University of
Science and Technology

Frida Xiang Nordås Årsandøy

Power optimisation of autonomous rotorcraft

Master's thesis in Industrial Cybernetics
Supervisor: Morten Dinhoff Pedersen
Co-supervisor: Finn Matras
June 2023

Norwegian University of Science and Technology
Faculty of Information Technology and Electrical Engineering
Department of Engineering Cybernetics

Sammendrag

Den raske veksten av droner de siste årene har muliggjort ulike bruksområder på tvers av forskjellige bransjer. Samtidig har Norge vedtatt European Aviation Safety Agency (EASA) regelverket som ble innført i 2021 for å regulere bruken av ubemannede luftfartøyer (UAV). Ettersom mange UAV-er er avhengige av batteri, er deres flytid begrenset. Derfor dukker det opp et rom for å optimalisere energiforbruket gjennom justeringer i UAV-flyhastigheten for å spare tilgjengelige energiressurser.

Hovedmålet med denne oppgaven er å undersøke kraftoptimalisering av multirotorer under foroverflyvning mens de overholder lovbestemmelser i ulike operasjonsscenarier. For å nøyaktig simulere kraftforbruk under flyging, vil studien benytte en nylig publisert innstrømningsmodell utviklet av Matras og Pedersen [1]. I motsetning til helikoptre med én rotor, har multirotorer flere tett plasserte rotorer som påvirker hverandre. Modellering av denne intrikate rotorinteraksjonen er avgjørende for presis kraftestimering, og er implementert uten tunge beregninger.

For å demonstrere anvendeligheten av simuleringsrammeverket av [1] for nåværende droneoperatører, ble relevante casestudier konstruert for å gjenspeile virkelige scenarier. Gjennom parameteridentifikasjon ble rammeverket dermed satt opp og tilrettelagt for å simulere de respektive multirotormodellene brukt for ulike scenarier.

Av de fire casestudiene som er presentert, viser resultatene at regulatoriske begrensninger kan komme til å påvirke den foreslåtte optimale flyhastigheten for minimalt kraftforbruk. Ved å justere UAV-ens foroverhastighet, kan maksimal flytid eller maksimal rekkevidde oppnås. Resultatene fra disse simuleringene kan hjelpe operatører med utvikling av energisparende strategier innenfor gjeldende UAV-regelverk. Videre legger resultatene grunnlaget for å inkludere flere scenarier og omfatte andre multirotorer.

Abstract

The rapid growth of drones in recent years has facilitated diverse applications across various industries. Simultaneously, Norway has adopted the European Aviation Safety Agency (EASA) regulations that were introduced in 2021 to govern the operation of unmanned aerial vehicles (UAVs). As many UAVs rely on battery power, their flight endurance is inherently constrained. Therefore, optimising energy consumption through adjustments in UAV flight speed emerges as a potential strategy to conserve available energy resources.

The primary objective of this thesis is to examine the power optimisation of multirotors during forward flight while complying with legal regulations in various operational scenarios. To accurately simulate power consumption during flight, the study will utilise a recently proposed inflow model developed by Matras and Pedersen [1]. Unlike helicopters with a single rotor, multirotors feature multiple closely positioned rotors that influence each other. Modelling this intricate rotor interaction is crucial for precise power estimation, and is embodied in the model without heavy computational effort.

To demonstrate the applicability of the simulation framework by [1] to current drone operators, relevant case studies were constructed to reflect real-world operating scenarios. Through initialising and parameter identification, the framework was thus set up and facilitated in order to simulate the respective multirotor models applied for different scenarios. Since the simulation framework offers scalability to existing drones with planar, non-overlapping rotors, valid simulations of power usage were conducted.

Of the four case studies presented, results show regulatory constraints influence the proposed optimal flying speed for minimised power consumption in half of them. By adjusting the UAVs forward speed, maximum flight time or maximum range can be attained. The insights gained from these results can help operators with the development of energy-saving strategies within current UAV regulations. Furthermore, the results lay the foundation to include additional scenarios and encompass other multirotor platforms, thereby facilitating further advancements in the field, especially with the new regulations arranging for larger UAVs, not necessarily operating in the very low-level (VLL) airspace.

Preface

This master's thesis is part of the subject TTK4900 - Engineering Cybernetics, Master's Thesis, worth 30 credits. It is being submitted as a partial fulfilment of the requirements for the 2-year master's degree program in Industrial Cybernetics at the Norwegian University of Science and Technology (NTNU). Throughout the course of this project, which has spanned the spring of 2023, I have been presented with a multitude of challenges, as well as invaluable opportunities for growth and new learning experiences. However, I believe that these past months have proven to be both insightful and rewarding for me.

Frida Xiang Nordås Årsandøy
June 5th, 2023

Acknowledgements

Apart from my very supportive and encouraging family, I have so far only encountered a handful of people who have truly left a profound and lasting impact on my path in life. The last and most recent addition to my list is my supervisor Morten Dinhoff Pedersen. This year, he took me under his wings by throwing me a lifebuoy when I found myself overwhelmed and struggling in way too deep water. For that, I am very grateful, in addition to his guidance during this last semester. He also introduced me to Finn Matras, who is an inspiration and has been laying the essential groundwork for me to conduct my master's thesis. So:

- Thank you, for your time
- Thank you, for sharing your knowledge with me
- And thank you, for being all the difference in my last semester at NTNU

One of my few regrets throughout my course of study is not switching to this master's thesis sooner, as it would have allowed me to benefit from their guidance in my specialisation project as well.

Last but certainly not least, I would also like to express my gratitude to the following list for sparing their valuable time for me amidst their already busy schedules:

- Karine Borgerud, my longtime friend, previous Bachelor-partner and current inspector of the Norwegian CAA for unmanned aerial vehicles, for your helpful input and feedback on my report
- Vegard Stien, professional drone pilot, for his continuous support and help to collect valuable data from several drone flights
- Daniel Kvalsund, police chief inspector and supervisor for Dronetjenesten Troms, for enhancing my understanding and knowledge regarding the police's use and practice during SAR operations with drones
- DJI, drone manufacturer, for providing supplementary information about their drones

Contents

List of Tables

List of Figures

Nomenclature

AGL	Above Ground Level
AOA	Angle of Attack
ARC	Air Risk Class
ATM	Air Traffic Management
BSL	Bemannet Sivil Luftfart
BVLOS	Beyond Visual Line Of Sight
CAA	Civil Aviation Authority
CFD	Computational Fluid Dynamics
CG	Center of Gravity
CO	Coordinate Origin
ConOps	Concept of Operation
DAA	Detect And Avoid
DOF	Degrees Of Freedom
EASA	European Union Aviation Safety Agency
EO	Electro-Optical
EU	European Union
EVLOS	Extended Visual Line Of Sight
GRC	Ground Risk Class
I2	Inspire 2

NOMENCLATURE

I3	Inspire 3
ICAO	International Civil Aviation Organisation
IPOPT	Interior Point OPTimizer
IR	Infrared
JARUS	Joint Authorities for Rulemaking on Unmanned Systems
LUC	Light UAS Operator Certificate
M300	Matrice 300 RTK
MTOM	Maximum Take-Off Mass
NAA	National Aviation Authority
NASA	National Aeronautics and Space Administration
NSM	National Security Authority
OM	Operations Manual
OSO	Operational Safety Objective
P mode	Position mode
P3	Phantom 3
PDRA	Predefined Risk Assessment
RO	RPAS Operator
RPM	Revolutions Per Minute
S Mode	Sports mode
SAIL	Specific Assurance Integrity Level
SAR	Search And Rescue
SORA	Specific Operation Risk Assessment
STS	Standard Scenarios
TMPR	Tactical Mitigations Performance Requirements
UA	Unmanned Aircraft

UAS	Unmanned Aircraft System
UAV	Unmanned Aerial Vehicle
UN	United Nations
VLL	Very Low-Level
VLOS	Visual Line Of Sight
VTOL	Vertical Take-Off and Landing

1 Introduction

In recent years, rotary wing unmanned aerial vehicles (UAVs) have attracted more interest due to the wide range of applications they can address, including research, commercial and recreational use. Among the promising applications that have emerged are package delivery, cinematography, agriculture and inspection [11, p. 215].

However, these applications are still somehow restricted since the available embedded energy, whose source often is Li-Po batteries, is limited. Since multirotors are heavier-than-air vehicles that rely on several rotors to generate lift, a significant proportion of the available energy is expended in sustaining the weight aloft. As a result, the energetic cost of flying remains a primary challenge, leading to incomplete mission assignments [12, p. 1423]. Moreover, new UAV regulations are currently being implemented in the European Union (EU), including Norway, which provide general guidelines and restrictions for drone operators [7]. Therefore, completing drone missions efficiently and conserving power while adhering to legal regulations is crucial.

In 2018, Pedersen proposed a novel method for describing inflow in multirotor systems, which was thereafter implemented by Matras [13]. In 2023, Matras and Pedersen published their modelling approach, which in forward flight, predicted a 60% increase in induced velocities at the rear rotors compared to when the rotors operated in isolation [1, p. 1]. This approach enables the computation of energy-optimal thrust allocation without the need for computationally intensive fluid dynamics (CFD) analysis. The findings from [1] yield less waste of energy and can then be applied to enhance the performance of multirotors already used by operators in various industries and disciplines.

This project will make use of the framework to minimise the waste of energy and provide practical examples of its operational uses. The aim is to showcase the inflow model's potential benefits in real-world settings, thereby bridging the gap between theoretical research and practical application. By showcasing the model's applicability for a selection of different case studies of relevance to the current drone industry, the research seeks to provide insight that can inform future energy-saving strategies within current UAV regulations.

1.1 Motivation

Figure 1.1 provides an informative visualisation of the interconnections between the optimisation problem, drone regulations, and physics, illustrating how the optimisation problem is linked to the cost function along with both physics and regulatory constraints. This visualisation serves as an overview of the factors involved in optimising energy mission planning, highlighting the integration of various elements.

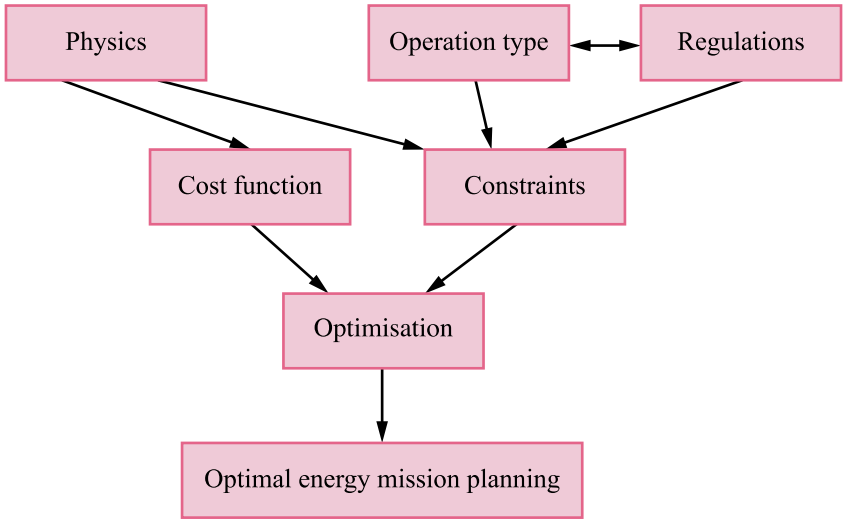

Figure 1.1: Interconnections between optimisation problem, cost function, constraints and drone regulations

The model takes into account a range of physical parameters to describe the drone's characteristics, such as mass, size, rotor configuration, and power consumption. These parameters serve as constraints that enforce the laws of physics and relationships between different variables. The model also uses a combination of linear and nonlinear constraints to ensure that the drone operates within the boundaries of the laws of physics. In summary, the physics constraints can be listed as follows:

- Nonlinear equality constraints for the drone model, specifically for the body frame velocity of the drone in x and z directions, which are constrained by the pitch angle θ indicating the drone's orientation and the velocity in the x-direction
- Nonlinear constraints to ensure the horizontal forces in body coordinates cancel out. The lift generated by the propellers must balance the gravitational force, as well as the generated thrust must be sufficient to counteract the drag. This is later illustrated in Chapter 2

- Nonlinear constraints are required for the rotational speed of the propellers. Additionally, linear constraints are needed for the torque applied by each propeller around the z-axis. as well as a linear constraint to ensure the sum of torques around the z-axis is zero

- The inflow model has several nonlinear constraints related to inflow conditions, specifically inflow angle χ, torques τ and moments Mz experienced by the rotors, and thus important for modelling the behaviour of the drone's rotors and their interaction with the surrounding airflow

- Power equality constraints that must be satisfied, specifically parasitic, profile and induced power, used for power calculations of the drone. These will be discussed later in Chapter 3 regarding power

Additionally, the constraints could also be influenced by regulatory conditions. Operation type will greatly depend on the operation purpose. For drone operations with public law purpose character, regulations about civil state aviation will apply, whereas commercial purposes require other regulatory conditions depending on the level of risk associated with the activity. As a result, the optimisation problem may be directly or indirectly constrained by several factors listed as follows:

- Maximum speed

- Maximum flight height above ground level (AGL)

- Safety distances, such as the ground risk buffer

The regulatory constraints will eventually be implemented as an inequality constraint on the following form, where V_{ix} represents the speed in the x-direction in the inertial frame and $V_{\max}$ is the maximum allowable speed.

$$0 \leq V_{\mathrm{ix}} \leq V_{\max} \tag{1.1}$$

Finally, the optimisation problem can be solved by minimising total power losses while considering all constraints. This approach will provide optimal values for pitch θ and speed V_{ix}.

1.2 Research agenda

The research was devoted as follows:

- Identify realistic drone case studies where minimisation of power loss is of relevance and operational advantage
- Parameter identification and validation of the model
- Optimisation and simulation of case studies where both physics and regulatory constraints are taken into account

1.3 Objectives

The topic can be divided into three categories. Firstly about the formulation of multirotor modelling and control allocation. The second category regards minimising available power losses with the aim to:

- Maximise flight time
- Maximise travel distance

The third category revolves around the Norwegian drone regulations in Norway, which first were implemented back in 2016 in Norway, and how findings and optimisation results can be aligned with the legislation in mind. That is, how utilisation of these techniques can bring benefits to drone operations in various industries by minimising energy losses. Specific scenarios will be given as examples to give insight to reduce the gap between theoretical research and practice.

1.4 Outline

Short overview of the structure of the report.

Chapter 1 - Introduction

Chapter 1 is an introductory chapter and is intended to present fundamental material to provide some introductory insight. UAVs, drag and power performances will be mentioned. In addition, the section will present background insight into the regulatory framework surrounding civil drones in Norway. The structure of authorities enforcing these regulations will also be accounted for to give a comprehensive understanding of the regulatory landscape that drone operators need to navigate. Towards the end previous work done regarding the power optimisation field will be briefly summarised. Lastly, contributions will be carefully listed.

Chapter 2 - Multirotor modelling

Chapter 2 will revolve around the modelling of the quadcopter, its fly physics and its equilibrium state. Additionally, the control allocation matrix will be derived and illustrated.

Chapter 3 - Power analysis

Causes of power consumption in flight will first be presented, as well as formulation of optimisation problems in order to optimise the flying speed in forward flight to achieve minimum power loss both for maximum flight time and maximum range.

Chapter 4 - Regulations on aviation with unmanned aerial vehicles

Chapter 4 revolves around drone regulations in both Norway and the EU and provides information about navigating the legislation in Norway. The purpose of the chapter is to present basic knowledge relevant to the case studies in Chapter 5, and provide essential background material on the matter.

Chapter 5 - Case studies

Chapter 5 examines four different case studies, each presenting a unique operational scenario that reflects various aspects of the current drone regulations in Norway. The main objective of the chapter is to investigate how these regulations can affect the optimisation problem and how they can be integrated into the simulation framework. By analysing these case studies, the chapter will highlight the importance of complying with regulations while optimising drone operations to ensure both safety and efficiency.

Chapter 6 - Parameter identification and model validation

In Chapter 6, the method of procedure for identifying the parameters required by the modelling framework is well documented. This includes the use of DJI data sheets and test data from sources such as NASA and Xoar propellers.

Chapter 7 - Results

Chapter 7 presents the results, and discusses and evaluates findings. First validation of the mathematical model and its framework will be discussed, followed by simulations carried out. The operational constraints highlighted in the case studies in Chapter 5 are also considered here.

Chapter 8 - Conclusion

The conclusion is found in Chapter 8 towards the end of the report and cites key results. Suggestions for future work also are enclosed in this chapter.

1.5 Physics background

1.5.1 Types of UAVs

There exist several categories of UAVs, as shown in Figure 1.2 [14, 15, p. 7]. In this project, the multirotor type will be the focus scope, specifically the quadcopter.

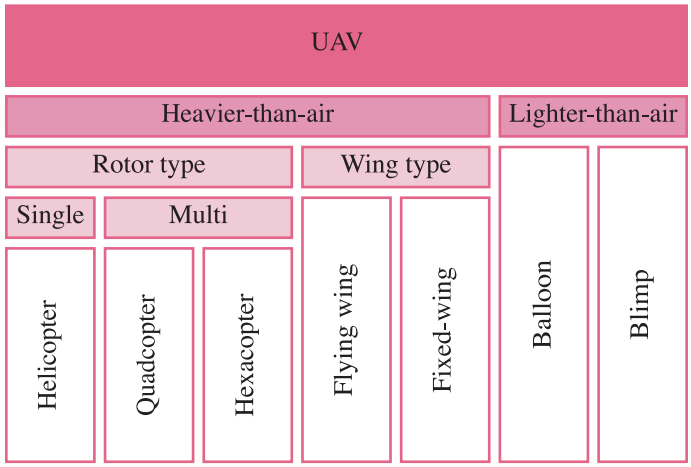

Figure 1.2: Overview of different types of UAVs

1.5.2 Multirotors

Multirotors, also referred to as multicopters, are types of UAVs or drones that utilise multiple rotors for lift and propulsion. They typically consist of a central frame with multiple rotors mounted, each driven by a separate electric motor. There are various configurations, such as quadcopters (four rotors), hexacopters (six rotors), and octocopters (eight rotors) [15]. Multirotors offer several advantages over fixed wings, including their ability to hover in place without requiring forward motion to generate lift, perform vertical take-offs and landings (VTOL), greater user-friendliness, and accessibility.

1.5.3 Power and drag

The relationship between power and drag is an important concept in aerodynamics. Power is the rate at which work is done or energy is transferred, while drag is a force that acts opposite to the motion of an object moving through a fluid (such as air). In general, as drag increases, a greater amount of power is necessary to overcome it.

During flight, multirotors are affected by three primary types of drag: parasitic drag, profile drag, and induced drag. The total drag is the sum of these three forces, which can be represented by a total drag curve. The minimum point on this drag curve signifies a speed where the total lift capacity of the multirotor, compared to its total drag, is most favourable. This factor is important for determining the performance of a multirotor [16, p.2-7].

Parasitic drag and power

Parasitic drag is comprised of form drag, interference drags and skin friction drag. Form drag is generated by the UAV due to its shape and airflow around it. Interference drag comes when intersections of airstreams arise as this can create eddy currents and turbulence, or possibly restricts smooth airflow. Skin friction drag arises due to the contact of moving air with the surface of the UAV [17, 5-6]. Thus parasitic drag will mainly be determined by the surface roughness, the object's shape, and the fluid's viscosity and density. Parasitic drag will rise as the airspeed is increased as well as reduced by streamlining the object's shape or reducing its surface roughness [18]. It mainly represents the loss produced by the actual body of the multirotor, excluding the propellers, in this project.

Parasite power is thus the power required to counteract the drag generated when the aircraft body, components that do not aid in lift generation, is moving through the air [19, p. 278]. As the speed of the drone increases, the parasite power, which is directly proportional to the cube of airspeed, experiences a substantial rise [20, p. 177].

Profile drag and power

Profile losses can be viewed as a specific form of parasitic drag, and be considered the parasitic drag of the wing or propeller [13, p. 21]. It is incurred from frictional resistance of the propellers passing through fluid, or in particular air. Equivalent to parasitic drag, profile drag will increase as forward speed is increased.

Profile power is thus defined as the power necessary to overcome the friction drag on the propeller blades and push the rotor's shape through the air [19, p. 278].

Induced drag and power

Induced drag is an inherent byproduct in the production of lift when an object moves through a fluid, such as air, and is a necessary trade-off in aerodynamics. When the propeller generates lift, there is a difference in pressure between the upper and lower surfaces of the blade, which can disrupt the flow of air over the wings, creating turbulence and drag [17, p. 5-7].

The pressure difference causes fluid to flow around the object, and this resulting motion of the fluid creates a wake [17, p. G-34]. The size and shape of the wake depend on the speed and size of the object and the properties of the fluid it is moving through. The presence of a wake can affect the performance of other objects or vehicles that are passing through the same fluid, as well as the stability and control of the object that created the wake [17, p. 6-6].

Induced power is thus the power that must overcome the drag developed during the creation of rotor thrust [19, p. 278]. At low speeds, induced drag can be a significant factor in power consumption, requiring a large amount of power just to maintain altitude and speed [17, p. 5-5]. One of the factors contributing to induced drag is the creation of wingtip vortices at the tips of the propellers. These swirling masses of air induce drag and increase power consumption. However, as the speed of the vehicle increases, the wingtip vortices become weaker and less pronounced, resulting in a decrease in induced drag [17, p. 5-8]. Consequently, less power is required to counteract the decreased induced drag, resulting in lower demand for induced power.

1.6 Regulatory background

1.6.1 Regulatory hierarchy

International Civil Aviation Organization (ICAO) is a specialised agency of the United Nations (UN) and is established to develop and promote cooperation on international civil aviation standards and recommended practices on a global level. Nevertheless, ICAO is not a global regulator and therefore primacy of national regulatory requirements always takes precedence over international standards. As of now, there are 193 members, including Norway [21].

European Union Aviation Safety Agency (EASA) is the EU's aviation safety agency responsible for setting and enforcing common safety standards for all EU member states. The responsibilities include drafting aviation safety legislation, providing technical advice, certifying and approving airworthiness and type certification of aircraft and aircraft parts for aircraft operating in the EU [22]. As of now, EASA member states consist of 27 EU

countries, along with Iceland, Liechtenstein, Norway, and Switzerland [23]. Since 2021, Norway has adopted EASA's rules in order to achieve common European regulations [24].

Further, each country has its own National Aviation Authority (NAA). In Norway, this is the Norwegian Civil Aviation Authority (CAA), which is responsible for regulating, inspecting and supervising aviation activities in Norway [25]. The Norwegian CAA has largely adapted to both regional and global guidelines and regulations and implemented both ICAO and EASA standards in its regulation of aviation activities.

In Figure 1.3, an overview of the connections between global, regional and national regulatory actors for civil unmanned aviation in Norway. Essentially, the CAA is responsible for regulating unmanned civil aviation in Norway, Avinor provides air traffic services and sets rules and regulations for flying UAVs close to airports, National Security Authority (NSM) decides prohibition areas for airborne sensor systems while the Norwegian Environment Agency determines protected areas with associated restrictions. In conclusion, operators must deal with multiple instances and gain an understanding of the legal and regulatory landscape in order to efficiently collect data or perform a diverse range of tasks. Furthermore, the Norwegian Data Protection Authority has established general regulations, although not exclusively for data collected from the air, regarding the collection of personal information that should be taken into consideration in certain circumstances.

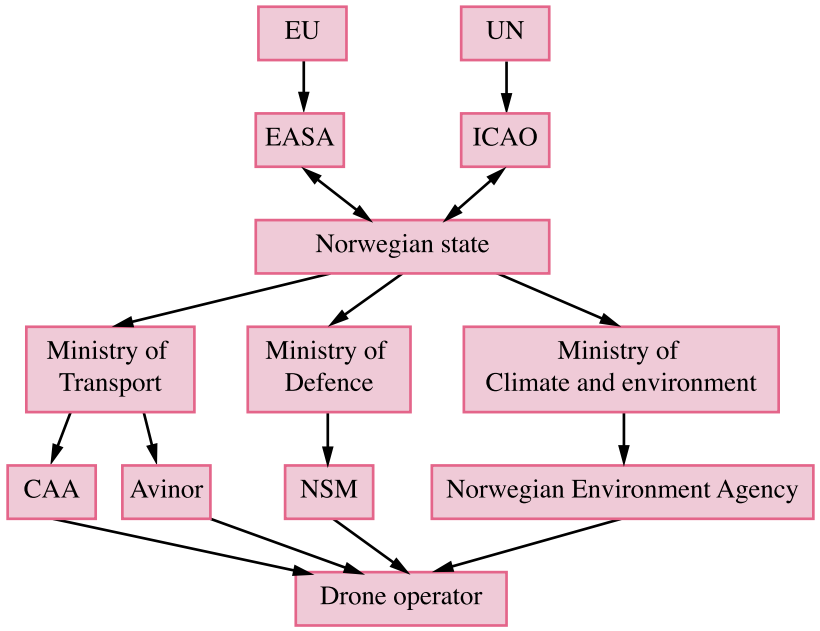

Figure 1.3: Overview of the global, regional, and national entities that civil drone operators must comply with

1.6.2 Operations manual

Similar to civil manned aviation, an operations manual (OM) is required in unmanned aviation for operators who wish to undertake operations associated with a higher level of risk. The OM is the governing document for an aviation operator [26] and is a comprehensive document that describes the standard operating procedures for the safe and efficient operation of drones. It mainly serves as a reference for pilots and personnel and is designed to ensure that operations are conducted in compliance with regulations and safety standards. Its contents usually include the concept of operations (ConOps) where the nature of the operation and associated risks are described, pilot training and qualifications, maintenance procedures as well as risk assessments and emergency response plans [26].

In addition to an OM, drone operators must choose a category to operate within based on risk assessment related to the drone operations to be approved by the CAA. These are named open, specific and certified respectively [7]. The chosen category will depend on the type of drone being used as well as its intended purpose.

1.6.3 Open, specific and certified categories

A simplified overview of the categories and their contents can be viewed in Figure 1.4. Open is considered low-risk operations and drones can therefore be flown without prior authorisation from the CAA. However, operational rules must be abided by operators as well as mandatory registration and a basic online course on drone safety. Although an OM is not mandatory, there are requirements on procedures adapted to the activity and complexity of the firm [27]. Normally, simpler visual line of sight (VLOS) operations fall within this category.

Drones operated in the specific category are considered to pose a higher risk and therefore require prior authorisation from the CAA. The authorisation can be obtained through a simplified procedure if the purpose can be categorised as a predefined commercial purpose [28]. Operations requiring larger-sized drones, which also typically are bearing payloads such as different camera equipment, fall into this category as well as beyond visual line of sight (BVLOS) operations. Examples include monitoring of sulfur emissions from ships [29] and plant stand count in agriculture [30]. Overall, the operational rules for the specific category can be seen as more restrictive than those for the open category.

The certified category caters for the operations with the highest level of risk and also requires operators to be certified prior to operations by the CAA [31]. Certified is intended for larger drones, similar to helicopters or airplanes, used for commercial purposes such as the transportation of goods or people. The air taxi will likely fall into this category. However, the implementation is not yet completed and it is reasonable to assume the process will be time-consuming as even EASA has yet to publish considerate material [8].

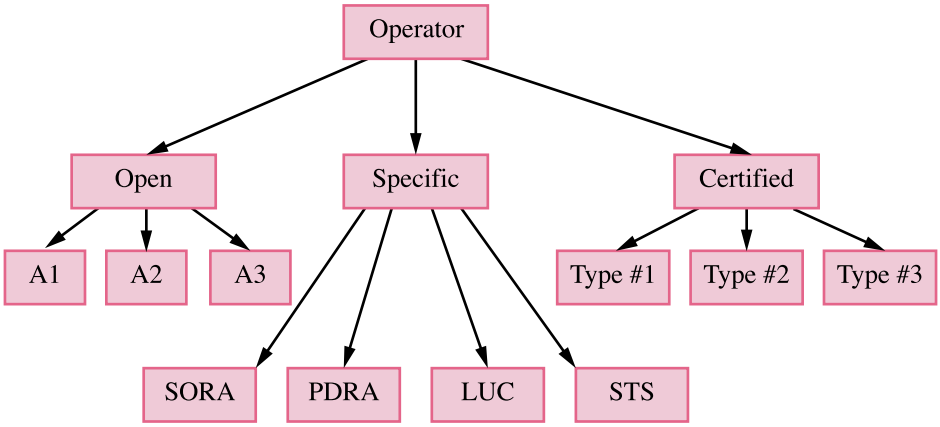

Figure 1.4: Simplified version of the possible categories for drone operators to be classified in for operations in accordance with BSL A 7-2

1.6.4 Definitions for flight operations

The following key terms portrayed in Figure 1.5 can be applied in calculations in order to undergo risk assessment [32, p. 28]. In this project, some of these boundaries will assist as constraints in the optimisation problem.

Flight geography

The volume the operator plans to conduct the operation in following normal procedures [32, p. 27].

Flight geography area

The area of the Earth's surface onto which the flight geography volume is projected is referred to as the flight geography area [32, p. 27].

Contingency volume

Contingency volume is defined as the volume where the operator needs to apply contingency procedures in order to bring the unmanned aircraft (UA) back to a normal situation within the flight geography [32, p. 27].

Contingency area

The contingency area is the projection of the contingency volume on the surface of the Earth [32, p. 27].

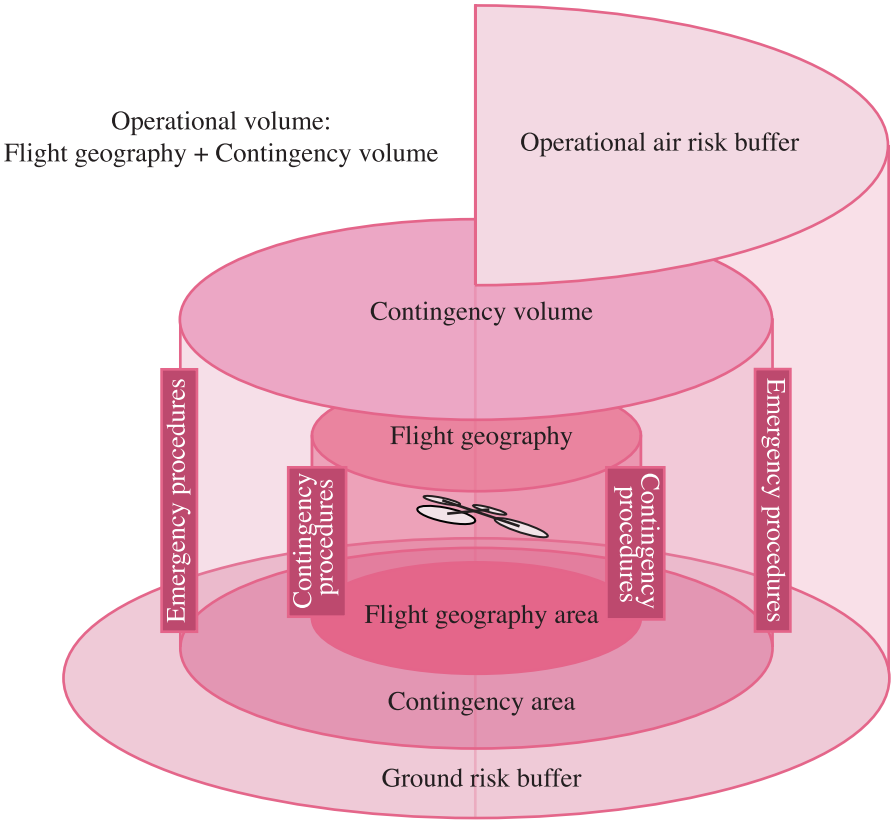

Figure 1.5: Definitions and relationship between different operational volumes and buffers

Operational volume

The operational volume consists of the flight geography and the contingency volume [32, p. 27].

Ground risk buffer

The ground risk buffer is a designated area on the Earth's surface surrounding the operational volume of the UAS. This buffer zone is established by the operator to mitigate potential risks to third parties on the ground in the event that the UA exits the operational volume [32, p. 27]. In the SORA methodology, the "1-to-1 rule" (1:1) is the standard method used to control ground risk, whereby the minimum ground risk buffer is equivalent to the height of the UAV AGL.

Air risk buffer

An air risk buffer is established in order to protect third parties in the air outside the operational volume [32, p. 224].

1.7 Previous work

Various efforts have been conducted to extend the flight duration of rotary wing unmanned aerial vehicles (UAVs). The existing research has among other things focused on the following aspects:

- Enhancing power to weight rate by reducing the weight of the UAV, such as the use of carbon fiber airframes and high energy density intelligent-soft materials [11, p. 215]
- Reducing energy consumption and increasing UAV endurance, with a primary focus on designing automated battery recharging or replacement systems [33]
- [34] proposed an optimisation model focused on minimising energy consumption and maximising battery lifetime for a low-power drone by transition strategy from the normal phase to the energy-saving phase to ensure the safe landing of the drone.

However, little to no work was found regarding the optimisation of power usage through the analysis of inflow power consumption. Additionally, there is a gap in research that considers both performance enhancement and adherence to regulatory requirements.

One study worth mentioning is [12], where Gandolfo evaluated the relationship between navigation speed and energy consumption in a miniature quadcopter, which follows a predefined path through experimental testing. The results show the speed control law can lead to 24 % extra path coverage for a fixed time while using 25% less energy when flown for a fixed distance [12, p. 1430].

Furthermore, Murray and Chu [35] highlighted the relationship between speed and flight endurance (range). Their analysis assessed the trade-offs between increased flight speed and longer flight endurance. The findings suggest that the travel speed of a drone plays a crucial role in drone delivery operations, as it directly impacts its range. The study concludes that higher speeds are favoured for drone package delivery, even if they result in a lower flight time [35, p. 105].

Nevertheless, exactly which speed is optimal, is not specified or suggested in either study. The studies do not consider different drone models differing in size and available energy either. Regulatory considerations nor regard were mentioned. These are aspects with which this report will concern itself.

1.8 Contributions

In this report, the following contributions have been made:

- Get the Matras' simulation framework set up and facilitated in order to enable simulations with the respective multirotor models
- Show and demonstrate the existence of potential energy savings in the available energy of multirotors by the usage of the inflow model by [1]
- By identifying and constructing relevant drone case studies and associated description and practice, exemplify how the simulation framework can be of use for drone operators and thus show its applicability value for real-life practices
- Based on optimisation results with simulation framework, highlight advantages and how this information can be used to strategically plan drone operations more effectively

2 Multirotor modelling

This chapter will begin by presenting and illustrating the four primary forces acting on a multirotor. The drag equation will also be introduced, along with the relevant coordinate systems and the six degrees of freedom (6-DOF) kinematic and kinetic equations. Additionally, the equilibrium state of the multirotor will be derived, and control allocation be accounted for.

2.1 Forces and torques

The UAV is typically composed of six elements that must be controlled in order to fly, three forces and three torques. Motions in x, y and z directions are surge, sway and heave respectively, The roll ϕ, pitch θ and yaw ψ torques cause the UAV to rotate around its longitudinal, lateral and vertical axis, respectively [2, p. 18]. The UAV can be assumed a rigid body which is capable of motion in six different directions, 6 DOFs where three are linear and three are angular.

Forces acting on the aircraft are lift F_L, weight F_G, thrust F_T and drag F_D. Firstly, lift is the upward force that opposes the weight of the UAV and keeps it in the air. Secondly, the weight is the force due to gravity acting, and thirdly thrust is generated by the propellers to propel the UAV forward. Lastly, drag is a rearward force caused by airflow disruption by the propellers and vehicle body [17, p. 5-1]. In steady forward flight, with no change in airspeed or vertical speed, these four forces must be in balance [16, p. 2-17].

To control the orientation of a multirotor drone, for example, a quadcopter with four rotors, the speed of certain rotors must be speed-up or slowed down. In Figure 2.1, a free-body diagram of a quadcopter is shown with identified forces. Propeller force, or thrust force, is marked with $F_{1,2,3,4}$ and lift F_L respectively, while gravitational force is assigned F_G. The rearward force representing the drag force is F_D. The distance from the rotor to CO, which is placed in CG, is marked with l.

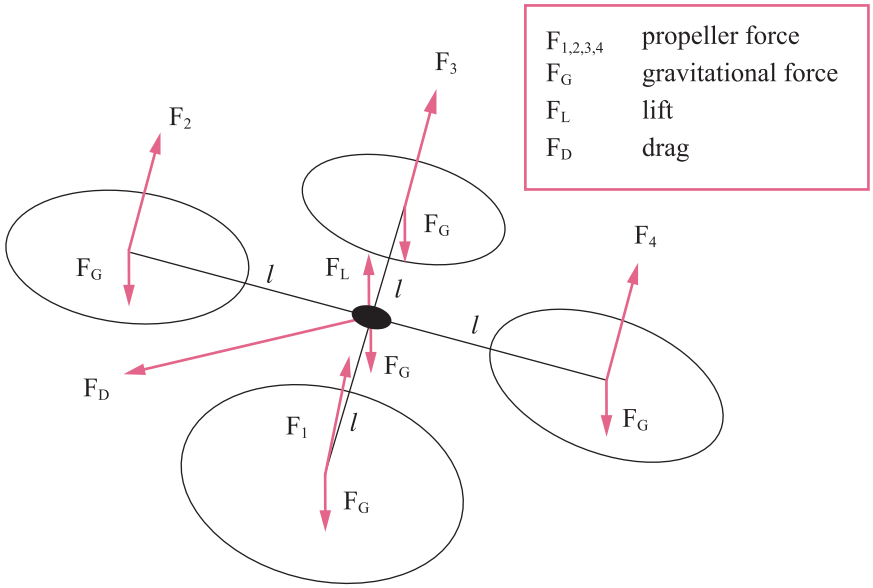

Figure 2.1: Free body diagram of a quadcopter

2.1.1 Propeller forces

Each propeller generates aerodynamic forces, a thrust force $f_{p,i}$ along the propeller's axis and a drag τ_d acting around the propeller axis. The steady-state thrust and drag generated by the i-th propeller modelled in equation (2.1) and (2.2) respectively, where k_t and k_d are constants of thrust and drag coefficients [36, p. 3]. Equation (2.1) represent the idealised case, where the propeller operates without any loss of efficiency.

$$f_{p,i} = k_t|\omega_i|\omega_i \tag{2.1}$$

$$\tau_i = k_d|\omega_i|\omega_i \tag{2.2}$$

2.1.2 Drag

The drag equation can be viewed in equation (2.3) [17, p. 5-5].

$$F_D = \frac{1}{2}\rho A C_D v^2 \tag{2.3}$$

$\frac{1}{2}$ is a constant, ρ is the air density, A is the front-facing area that is directly into the oncoming airflow, C_D is the aerodynamic drag coefficient, and v the relative speed [20, p. 177]. The drag coefficient depends on the shape of the drone and the orientation of the obstructing surface.

An overview of drag coefficients for different object shapes can be viewed in Table 2.1 [37, p. 237]. In the report, the drone will be treated as a facing cube.

Table 2.1: Overview of drag coefficients for object shapes

Shape	C_D
Sphere	0.47
Cube, edge on	0.8
Cube, face on	1.05

2.2 Coordinate systems

To obtain a mathematical model, two coordinate systems are defined:

- Body fixed frame - $\mathcal{F}^B$
- Inertial frame - $\mathcal{F}^I$

where the quadcopter position is defined by x, y and z in $\mathcal{F}^{\mathcal{I}}$, while ϕ, θ and ψ are expressed as rotations about x_b, y_b and z_b respectively [2, p. 18]. $\mathcal{F}^B$ is fixed to the quadcopter body and has its positive x_b direction in the forward direction of the drone, y_b towards its left arm and z_b in upwards direction. $\mathcal{F}^B$ has its CO in CG. $\mathcal{F}^I$ is considered to be fixed relative to the Earth's surface and does not rotate with the Earth. An illustration of a quadcopter with coordinate systems is depicted in Figure 2.2.

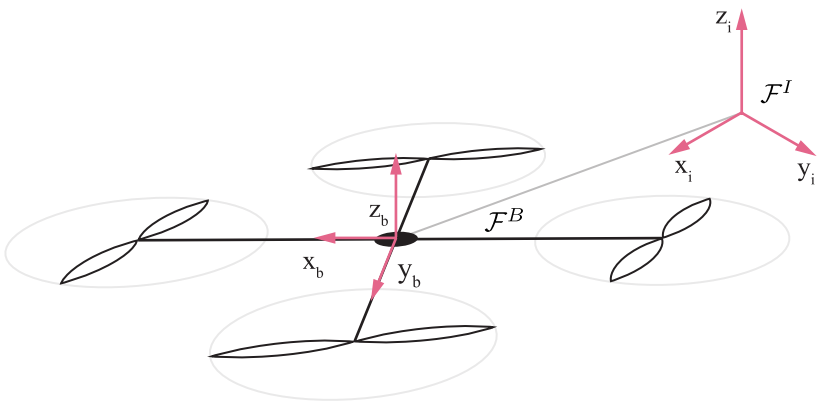

Figure 2.2: Quadcopter coordinate systems

2.3 Kinematics and kinetics

The 6-DOF kinematic and kinetic equations can then be expressed as (2.4) and (2.5) respectively [2, p. 31, p. 64].

$$\dot{\boldsymbol{\eta}} = \mathbf{J}(\boldsymbol{\eta})\boldsymbol{\nu} \tag{2.4}$$

$$\dot{\boldsymbol{\nu}} = \mathbf{M}^{-1}\Big(\boldsymbol{\tau}(\boldsymbol{\nu}) - \mathbf{C}(\boldsymbol{\nu})\boldsymbol{\nu}\Big) \tag{2.5}$$

2.3.1 Kinematic equation

For multirotor in 6-DOFs, the generalised position depicted in (2.6) can be chosen [2, p. 22].

$$\boldsymbol{\eta} = \begin{bmatrix} x_i & y_i & z_i & \phi & \theta & \psi \end{bmatrix}^T \tag{2.6}$$

The generalised velocity vector is denoted as (2.7) in $\mathcal{F}^B$ [2, p. 22].

$$\boldsymbol{\nu} = \begin{bmatrix} u & v & w & p & q & r \end{bmatrix}^T \tag{2.7}$$

However, for forward motion in x-direction and considering only non-rotational states, simplifications in equation (2.8) can be done since linear motion mainly will be considered.

$$\boldsymbol{\nu} = \begin{bmatrix} u & v & w & 0 & 0 & 0 \end{bmatrix}^T \tag{2.8}$$

The transformation matrix $\boldsymbol{J}(\boldsymbol{\eta})$ that can be given as (2.9) [2, p. 31].

$$\boldsymbol{J}(\boldsymbol{\eta}) = \begin{bmatrix} \mathbf{R}_b^i & \mathbf{0}_{3\times3} \\ \mathbf{0}_{3\times3} & \mathbf{T}_b^i \end{bmatrix} \tag{2.9}$$

Rotations and transformations of velocities and angular rates from $\mathcal{F}^B$ to $\mathcal{F}^I$ is shown in (2.10) and (2.11) respectively, where c, s and t are shortened for $\cos$, $\sin$ and $\tan$ [2, p. 28, p. 29].

$$\mathbf{R}_b^i = \begin{bmatrix} c\psi c\theta & -s\psi c\phi + c\psi s\theta s\phi & s\psi s\phi + c\psi c\phi s\theta \\ s\psi c\theta & c\psi c\phi + s\psi s\theta s\psi & -c\psi s\phi + s\theta s\psi c\phi \\ -s\theta & c\theta s\phi & c\theta c\phi \end{bmatrix} \tag{2.10}$$

$$\mathbf{T}_b^i = \begin{bmatrix} 1 & s\phi t\theta & c\phi t\theta \\ 0 & c\phi & -s\phi \\ 0 & \frac{s\phi}{c\theta} & \frac{c\phi}{c\theta} \end{bmatrix} \tag{2.11}$$

2.3.2 Kinetics for rigid body equation

$\mathbf{M}$ is the mass matrix, $\mathbf{C}$ is the Coriolis centripetal matrix, and $\boldsymbol{\tau}$ the total vector of external forces and moments expressed in $\mathbf{F}^B$ [2, p. 55]. $\mathbf{M}$ is given in (2.12), where m is the UAV mass, $\mathbf{I}_3$ the identity matrix, and $\mathbf{I}$ is the moment of inertia defined in (2.13) [2, p. 64].

$$\mathbf{M} = \begin{bmatrix} m\mathbf{I}_3 & \mathbf{0}_{3\times 3} \\ \mathbf{0}_{3\times 3} & \mathbf{I} \end{bmatrix} \tag{2.12}$$

Assuming the quadcopter frame has a symmetrical structure where rotor arms are aligned with the x_b- and y_b axes, the inertia matrix becomes a diagonal matrix $\mathbf{I}$ where I_x = I_y [38, p. 91].

$$\mathbf{I} = \begin{bmatrix} I_x & 0 & 0 \\ 0 & I_y & 0 \\ 0 & 0 & I_z \end{bmatrix} \tag{2.13}$$

$\mathbf{C}$ is given as a simplified version in (2.14) [2, p. 67].

$$\boldsymbol{C}(\boldsymbol{\nu}) = \begin{bmatrix} 0 & 0 & 0 & 0 & mw & -mv \\ 0 & 0 & 0 & -mw & 0 & mu \\ 0 & 0 & 0 & mv & -mu & 0 \\ 0 & -mw & mv & 0 & I_z r & -I_y q \\ mw & 0 & -mu & -I_z r & 0 & I_x p \\ -mv & mu & 0 & I_y q & -I_x p & 0 \end{bmatrix} \tag{2.14}$$

The sum of identified forces and moments is represented by $\boldsymbol{\tau}$ in (2.15), where the actuators, propellers, are represented by $\boldsymbol{\tau}_{\mathrm{act}}$, gravity given by $\boldsymbol{\tau}_{\mathrm{g}}$, and the resistance of moving the vehicle through a fluid by $\boldsymbol{\tau}_{\mathrm{res}}$ [13, p. 28].

$$\boldsymbol{\tau} = \boldsymbol{\tau}_{\mathrm{act}} - \boldsymbol{\tau}_g - \boldsymbol{\tau}_{\mathrm{res}} \tag{2.15}$$

The total forces and moments generated by the actuators given by $\boldsymbol{\tau}_{\mathrm{act}}$ is stated in (2.16) [13, p. 54]. It is assumed that the thrust is solely along the z-direction, and the drag is due to rotations around this axis, allowing for simplifications. Here, nr represents the number of propellers, and ω_i denotes the rotational speed of the i-th propeller while k_t and k_d are associated with the thrust and drag forces, respectively.

$$\boldsymbol{\tau}_{\text{act}} = \sum_{i}^{nr} \begin{bmatrix} 0 \\ 0 \\ k_t \\ 0 \\ 0 \\ k_d \end{bmatrix} \omega_i^2 \tag{2.16}$$

$\boldsymbol{\tau}_{\text{g}}$ is stated in (2.17), where g is the gravitational acceleration and m is the mass [13, p. 28].

$$\boldsymbol{\tau}_g = \begin{bmatrix} mg\sin\theta \\ -mg\cos\theta\sin\phi \\ -mg\cos\theta\cos\phi \\ 0 \\ 0 \\ 0 \end{bmatrix} \tag{2.17}$$

Furthermore, the resistance $\boldsymbol{\tau}_{\text{res}}$ is assumed linear and expressed as shown in equation (2.18), where R_u, R_v and R_w represent the resistance coefficients specific to the drone model [13, p. 28]. It is important to note that these coefficients will vary depending on the characteristics of the individual drone models.

$$\begin{aligned} \boldsymbol{\tau}_{\text{res}} &= \mathbf{R}\boldsymbol{\nu} \\ &= \begin{bmatrix} R_u & 0 & 0 & 0 & 0 & 0 \\ 0 & R_v & 0 & 0 & 0 & 0 \\ 0 & 0 & R_w & 0 & 0 & 0 \\ 0 & 0 & 0 & 0 & 0 & 0 \\ 0 & 0 & 0 & 0 & 0 & 0 \end{bmatrix} \boldsymbol{\nu} \end{aligned} \tag{2.18}$$

Then the kinetic equation from (2.5) can be reformulated, and the kinematic and kinetic equations can then be given as in (2.19) and (2.20) respectively.

$$\dot{\boldsymbol{\eta}} = \mathbf{J}(\boldsymbol{\eta})\boldsymbol{\nu} \tag{2.19}$$

$$\dot{\boldsymbol{\nu}} = \mathbf{M}^{-1}\Big(\boldsymbol{\tau}_{\text{act}}(\boldsymbol{\nu}) - \boldsymbol{\tau}_{\text{g}} - \boldsymbol{\tau}_{\text{res}}(\boldsymbol{\nu}) - \mathbf{C}(\boldsymbol{\nu})\boldsymbol{\nu}\Big) \tag{2.20}$$

2.4 Control allocation

Control allocation is the process of distributing generalised forces $\boldsymbol{\tau} \in \mathbb{R}^n$ given by $\boldsymbol{\tau} = \mathbf{Bu}$ to actuators with physical control inputs $\mathbf{u} \in \mathbb{R}^r$. This is illustrated in Figure 2.3 [2, p. 317]. The goal can be to achieve a desired flight path or manoeuvre by controlling the various systems that affect the drone's movement.

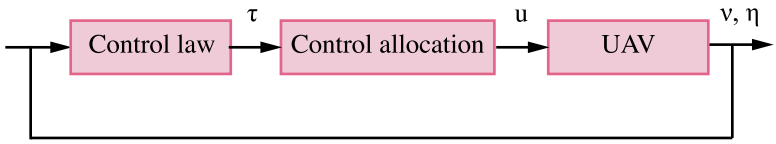

Figure 2.3: Control allocation loop as illustrated in [2, p. 317]

Equation 2.21 yields the mapping $\mathbf{B}$ between the desired moments $\boldsymbol{\tau}$ and total forces $\mathbf{T}$ to the required thrusts $f_{p,i}$ that each propeller must produce in order to generate the total force and achieve the desired moments. Here $\mathbf{T}$ represents the generalised force generated in the x, y and z-direction of the airframe, and consists of $\mathbf{T} = [F_x \ F_y \ F_z]^T$, while $\boldsymbol{\tau}$ presents the the generalised moment generated about x, y, z, and can be expressed as $\boldsymbol{\tau} = [\tau_x \ \tau_y \ \tau_z]^T$.

$$\begin{aligned} \boldsymbol{\tau} &= \mathbf{Bu} \\ \begin{bmatrix} \mathbf{T} \\ \boldsymbol{\tau} \end{bmatrix} &= \mathbf{B} \begin{bmatrix} f_{p,1} \\ f_{p,2} \\ f_{p,3} \\ f_{p,4} \end{bmatrix} \end{aligned} \tag{2.21}$$

2.4.1 Equilibrium

The multirotor flying at a constant speed in a horizontal moving state is an example of Newton's first law of motion $\sum F = 0$. In the equilibrium state, all forces cancel each other in order to produce no net force. This includes F_G, F_L, F_T, and F_D acting on the drone, as well as the ϕ, θ, and ψ moments. The upward lift equals the downward force of gravity, while the forward thrust of the propellers is matched by the backward drag on the multirotor. Thus the multirotor will continue to move in a straight line. If the forces generated by each propeller are not equal, it can cause the drone to drift or spin uncontrollably. Equation (2.22) is therefore presumed to hold.

$$F_1 = F_2 = F_3 = F_4 \Rightarrow F_i \tag{2.22}$$

In Figure 2.4 the decomposition of the quadcopter forces is illustrated.

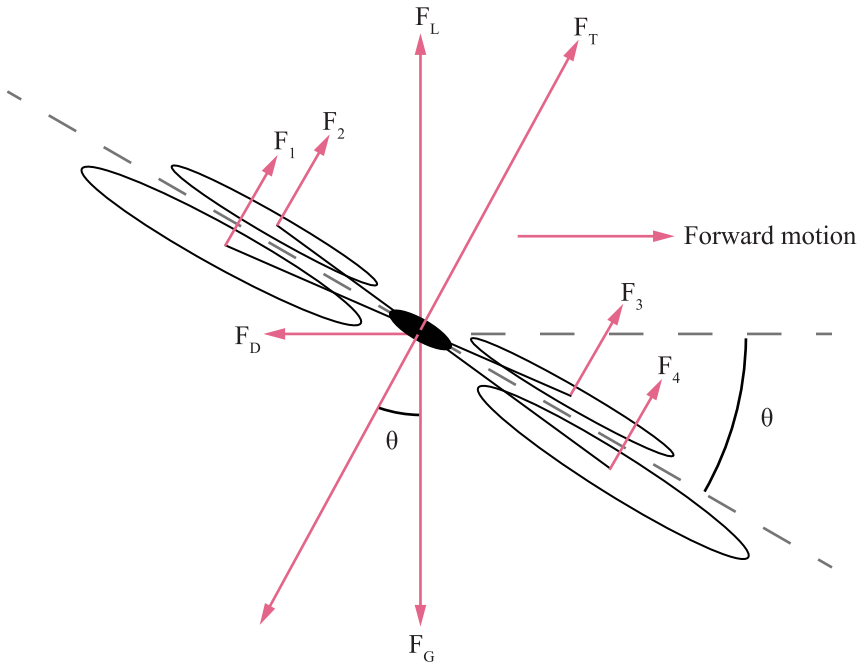

Figure 2.4: Illustration of the equilibrium state of quadcopter

Furthermore, it can be assumed equation 2.23 is true for F_T.

$$F_T = F_1 + F_2 + F_3 + F_4 = 4\,F_i \tag{2.23}$$

F_D can be found by calculating the forward thrust in equation 2.24, as it can be assumed drag is acting in continual opposition to forward motion and is equal in equilibrium.

$$\begin{aligned} F_D &= \sin(\theta) F_T \\ &= \sin(\theta) \underbrace{(F_1 + F_2 + F_3 + F_4)}_{4\,F_i} \\ &= 4F_i \sin(\theta) \end{aligned} \tag{2.24}$$

The force F_i provided by each propeller can be found as shown in equation 2.25 from F_G.

$$\begin{aligned} F_G &= \cos(\theta) \underbrace{(F_1 + F_2 + F_3 + F_4)}_{4\,F_i} \\ &= 4F_i \cos(\theta) \\ \Rightarrow F_i &= \frac{F_G}{4\cos(\theta)} \end{aligned} \tag{2.25}$$

For nr number of propellers, equation 2.26 is applied.

$$F_i = \frac{F_G}{nr\ \cos(\theta)} \tag{2.26}$$

The total force including all nr propellers $\mathbf{T}$ then becomes (2.27).

$$\begin{aligned} \mathbf{T} &= nr \cdot \frac{F_G}{nr\ \cos(\theta)} \\ &= \frac{F_G}{\cos(\theta)} \end{aligned} \tag{2.27}$$

When the quadcopter is hovering in a stable position, or alternatively flying forward on a straight path, it is desired that the moments τ_x, τ_y and τ_z are equal to zero. Thus, the quadcopter is not rotating around any of its principal axes but maintaining a stable orientation. Hence, it is assumed τ_x, τ_y and τ_z are equal to zero since the sum of all moments must be so in the state of equilibrium.

Combing the result in equation 2.27, result in equation 2.28.

$$\begin{bmatrix} \mathbf{T} \\ \tau_x \\ \tau_y \\ \tau_z \end{bmatrix} = \begin{bmatrix} \frac{F_G}{\cos(\theta)} \\ 0 \\ 0 \\ 0 \end{bmatrix} = \mathbf{B} \begin{bmatrix} f_{p,1} \\ f_{p,2} \\ f_{p,3} \\ f_{p,4} \end{bmatrix} \tag{2.28}$$

2.4.2 Forward flight equilibrium

In Figure 2.4 from the previous subsection, Subsection 2.4.1, it can be observed F_D and F_G can be decomposed as shown in equation (2.29), where $F_T = F_1 + F_2 + F_3 + F_4$.

$$\begin{aligned} F_D &= \sin(\theta) \cdot F_T \\ F_G = mg &= \cos(\theta) \cdot F_T \end{aligned} \tag{2.29}$$

Therefore, by dividing the equations in (2.29), the following equation in (2.30) is yielded.

$$
\begin{aligned}
tan(\theta) &= \frac{F_D}{mg} \\
mg \cdot \tan(\theta) - F_D &= 0 \\
mg \cdot \tan(\theta) - \frac{1}{2}\rho A C_D v^2 &= 0
\end{aligned}
\tag{2.30}
$$

By utilising Newton's method, the value for pitch angle θ can be obtained for a given speed v. Then the optimal pitch can be used in equation (2.28) which further be used to calculate the forces fed to each propeller by the control allocation matrix $\mathbf{B}$.

Determining the pitch θ is illustrated in Figure 2.5, where θ can be found when $F_{D,x}$ and $F_{G,x}$ are equal. Specifically, when the drag force component in the x-direction and the gravitational force component in the x-direction are equal, indicating a state of equilibrium in forward flight.

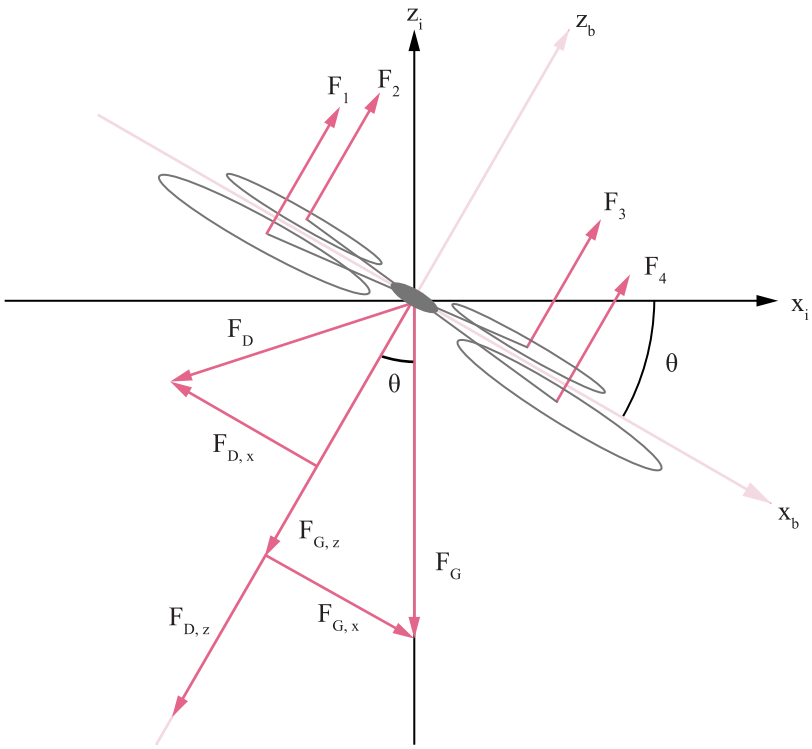

Figure 2.5: Optimal pitch angle θ can be found when $F_{D,x}$ and $F_{G,x}$ are equal

2.4.3 Derivation of the control allocation matrix

For a multirotor, a control allocation matrix must be obtained in order to distribute forces to the rotors in the system. The general setup is shown in equation 2.31, and then decomposed and multiplied in equation 2.32. Figure 2.6 shows an illustration of the decomposition.

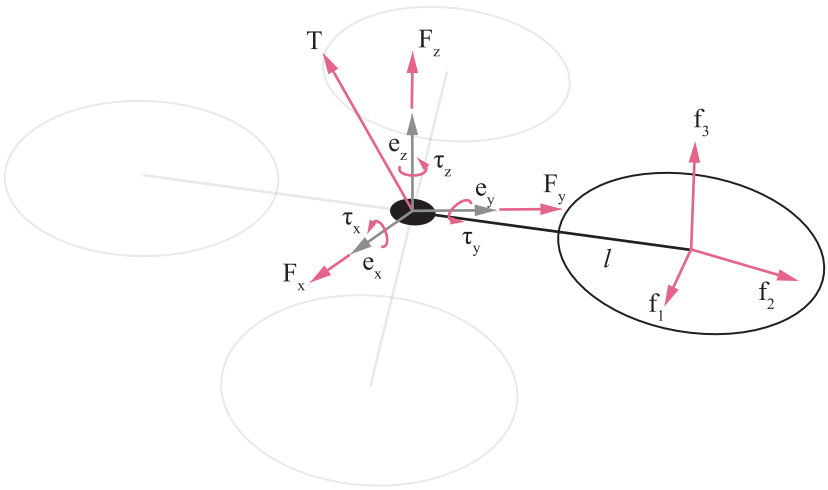

Figure 2.6: Illustration of forces decomposed

$$\begin{bmatrix} \mathbf{T} \\ \boldsymbol{\tau} \end{bmatrix} = \begin{bmatrix} \mathbf{I_3} & \mathbf{0}_{3\times3} \\ \mathbf{S(l)} & \mathbf{I_3} \end{bmatrix} \begin{bmatrix} f \\ t \end{bmatrix} \tag{2.31}$$

$$\begin{bmatrix} F_x \\ F_y \\ F_z \\ \tau_x \\ \tau_y \\ \tau_z \end{bmatrix} = \underbrace{\begin{bmatrix} 1 & 0 & 0 \\ 0 & 1 & 0 \\ 0 & 0 & 1 \\ 0 & -l_3 & l_2 \\ l_3 & 0 & -l_1 \\ -l_2 & l_1 & 0 \end{bmatrix}}_{\mathbf{B} = \text{control allocation matrix}} \begin{bmatrix} f_1 \\ f_2 \\ f_3 \end{bmatrix} \tag{2.32}$$

By simplifying Equation 2.32 to include the union between heave, roll, pitch, and thrust components, the relationship between the thrust force f_3 and the torque control inputs for heave, roll, and pitch, as expressed in equation (2.33), can be established. It can also be noted that the equation is derived for a single propeller.

$$\Rightarrow \begin{bmatrix} F_z \\ \tau_x \\ \tau_y \end{bmatrix} = \begin{bmatrix} 1 \\ -l_2 \\ l_1 \end{bmatrix} f_3 \tag{2.33}$$

To ensure proper distribution of control inputs among the available actuators and guarantee that the sum of control inputs matches the desired thrust, it is common practice to normalise the control allocation matrix. Specifically, the first column is normalised to a sum of one. In equation (2.35), the total force F is normalised for a multirotor with nr propellers. Notably, for roll and yaw control, these elements sum to zero because of the geometric symmetry of the multirotor system.

Yaw can also be included but is however modelled as in (2.34) where b, c and k represent constants. The result is ones with an alternating sign matching the rotational direction with respect to the right-hand rule [13, p. 61].

$$\begin{aligned} \tau_z &\approx \pm c|\omega|\omega \\ f_3 &\approx b|\omega|\omega \\ \Rightarrow \frac{\tau_z}{f_3} &\approx \pm\frac{c|\omega|\omega}{b|\omega|\omega} = \pm\frac{c}{b} = \pm k \end{aligned} \tag{2.34}$$

For four rotors the control allocation matrix is shown in equation (2.35). Propellers 1-4 are represented by p1, p2, p3, and p4 respectively.

$$\begin{bmatrix} F_z \\ \tau_x \\ \tau_y \\ \tau_z \end{bmatrix} = \underbrace{\begin{bmatrix} \frac{1}{nr} & \frac{1}{nr} & \frac{1}{nr} & \frac{1}{nr} \\ -l_{2,p1} & -l_{2,p2} & -l_{2,p3} & -l_{2,p4} \\ l_{1,p1} & l_{1,p2} & l_{1,p3} & l_{1,p4} \\ 1 & -1 & 1 & -1 \end{bmatrix}}_{\mathbf{B}} \begin{bmatrix} f_{3,p1} \\ f_{3,p2} \\ f_{3,p3} \\ f_{3,p4} \end{bmatrix} \tag{2.35}$$

2.4.4 Standard control allocation matrix

An alternative allocation matrix, shown in (2.36), can also be derived for nr numbers of rotors [13, p. 60]. Both matrices will still yield the same result.

$$\underbrace{\begin{bmatrix} \frac{1}{nr} & -l_1 \sin(\arctan(\frac{y_1}{x_1})) & l_1 \cos(\arctan(\frac{y_1}{x_1})) & 1 \\ \vdots & \vdots & \vdots & \vdots \\ \frac{1}{nr} & -l_{nr} \sin(\arctan(\frac{y_{nr}}{x_{nr}})) & l_{nr} \cos(\arctan(\frac{y_{nr}}{x_{nr}})) & -1 \end{bmatrix}}_{\mathbf{B}} \tag{2.36}$$

3 Power analysis

An important aspect of power analysis is the calculation of rotor forces and power losses during flight, as these losses can impact the performance and efficiency of the drone. Usually, power consumption is dependent on several factors, such as the type, weight and design of the UAV as well as the flight speed. In this chapter derivation of power consumption and description for multirotors will follow.

3.1 Power consumption in flight

Power is necessary to lift the drone off the ground and gain altitude. Additionally, power is required to counteract the parasitic drag that is hindering its forward movement through the air [20, p. 177].

The general equation of power can be formulated as equation (3.1) respectively [39], where P is the power given in watts (W), F the force in Newton (N) and v the speed and direction of motion of an object in meters per second (m/s).

$$P = Fv \tag{3.1}$$

Further, the total power P_{total} required for a single rotor in forward flight can be expressed as (3.2), where P_p is the parasitic power, P_f is induced power and P_i is the induced [40, p. 217].

$$P_{\text{total}} = P_p + P_f + P_i \tag{3.2}$$

The different power losses are simplified and illustrated in figure 3.1 respectively. The first and second figures are parasitic and profile losses due to the vehicle body and propellers moving through the fluid. In the third figure, the induced loss is depicted as the airborne quadcopter generates lift and redirects the airflow coming at it.

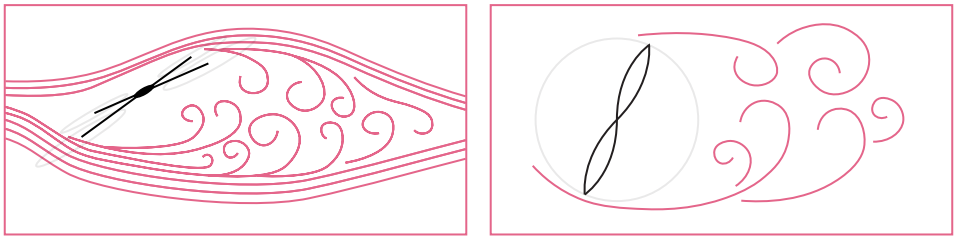

(a) Parasitic

(b) Profile

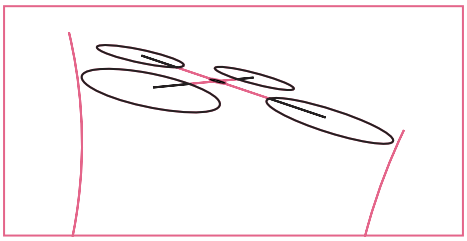

(c) Induced

Figure 3.1: Illustration of the different types of power losses

3.1.1 Parasitic losses

Using the drag equation (2.3), parasitic drag D_p can be modelled as in (3.3)

$$\begin{aligned} D_p &= \frac{1}{2}\rho A C_D v^2 \\ &= \frac{1}{2}\rho A C_D |v| v \end{aligned} \tag{3.3}$$

Hence, by combing the parasitic drag equation (3.3) and power equation (3.1), the power P_p required to overcome parasitic drag D_p of the vehicle body is (3.4).

$$\begin{aligned} P_p &= D_p v \\ &= \left(\frac{1}{2}\rho A C_D v^2\right) v \\ &= \frac{1}{2}\rho A C_D v^3 \end{aligned} \tag{3.4}$$

Since parasitic drag D_p is caused by friction between the vehicle body and fluid, the drag will increase as the speed increases. The faster the vehicle moves through the fluid, the more resistance it encounters due to friction. Therefore, the power P_p will increase in faster speed as well [20, p. 179].

3.1.2 Profile losses

Profile power losses P_f occur due to the drag of propellers of the drone in viscous fluid [19, p. 34]. Similar to parasitic power P_p, profile power P_f can be modelled as in (3.5) where D_f is the profile drag.

$$\begin{aligned} P_f &= D_f \omega \\ &= \left(\frac{1}{2} \rho A C_D |\omega| \omega \right) \omega \\ &= \frac{1}{2} \rho A C_D \omega^3 \end{aligned} \tag{3.5}$$

Profile drag is a subtype of parasitic drag, and the P_f will therefore also increase with faster speed.

3.1.3 Induced losses

Unlike parasitic drag, the induced drag D_i is associated with the generation of lift. When a propeller is producing lift during level flight, it incurs the penalty-induced drag that will gradually decrease as the speed of the vehicle increases [17, p. 5-6]. To properly capture the dynamics of inflow, the newly published inflow model proposed by Matras and Pedersen will be employed.

In 2023, Matras and Pedersen [1] presented a novel modelling approach that is derived from first principles by employing the linearised Euler equation in combination with Fourier analysis [1, p. 3]. Notably, what distinguishes this model is its comprehensive treatment of the intricate interactions among multiple rotors. In particular, it takes into account the interaction effect, which arises from the impact of the wake generated by one rotor on the flow conditions experienced by the other rotors in the system. This interaction effect plays a crucial role in the increased complexity of modelling multirotor systems compared to systems with only a single rotor [1, p. 1].

Based on the findings presented in [1], it has been observed that during forward flight of a quadcopter, the rear rotors experience a significant increase in mean induced velocity compared to the front pair [1, p. 1]. This is visually depicted in Figure 3.2b, where the rear rotors exhibit higher velocities compared to the front rotors. The observed increase in induced velocity for the rear rotors can be attributed to the rear rotors operating within a flow field that contains components of the induced velocity generated by the front rotors. Furthermore, [1, p. 1] conclude the rear rotors experience a 19% reduction in inflow skew. These findings highlight the substantial aerodynamic interaction between the rotors, which has a direct impact on the induced velocities, and consequently affects the power consumption of the system [1, p. 20].

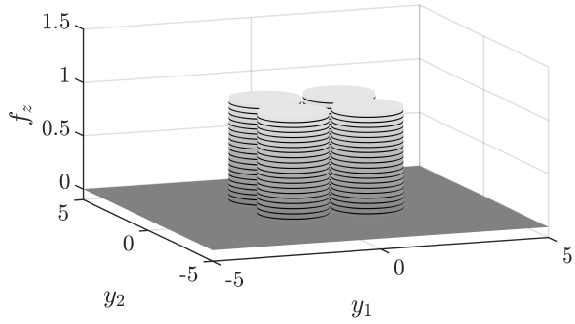

(a) Uniform thrust distribution

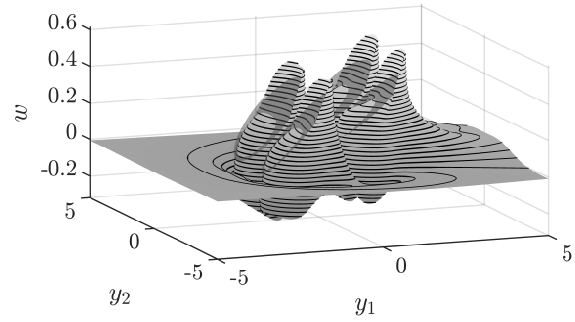

(b) Flow fields and the parameterizations of these fields portrayed as disks

Figure 3.2: Illustrations of quadrotor in forward flight (skew angle $\chi = 60°$) is reproduced with permission from Matras [1]

The multirotor steady-state inflow model is shown in equation (3.6). In this model, $\boldsymbol{\nu} = [\nu^1 \ \nu^2 \ \dots \ \nu^N]^T$ and $\boldsymbol{\tau} = [\tau^1 \ \tau^2 \ \dots \ \tau^N]^T$ correspond to the inflow and forces for N numbers of rotors, respectively [1, p. 12]. Furthermore, the $\mathbf{L}$ and $\mathbf{D}$ matrices represent the flow on each grey disk illustrated in Figure 3.2a, effectively describing the model's behaviour [1, p. 11].

Hence, the model offers a finite state reconstruction of the flow field while facilitating efficient inflow simulation with excellent computational efficiency [1, p. 12, p. 22]. Importantly, the approach employs an efficient parametrization, enabling the model to be formulated on a linear time-varying state-space form. This makes the model particularly well-suited for real-time applications that are involving multirotor dynamics, as well as stability and control problems [1, p. 1].

$$\boldsymbol{\nu} = \mathbf{L}\boldsymbol{\tau} + \mathbf{D}\boldsymbol{\tau} \tag{3.6}$$

Induced power losses P_i are thus calculated according to (3.7), where $\mathbf{T}$ represents the thrust and $\boldsymbol{\nu}$ denotes the inflow velocities. Neglecting this effect can lead to a power graph that shows a continuous increase as the speed rises, failing to accurately capture power usage, especially at lower speeds where induced power is at its maximum. Therefore, considering induced power is crucial for the comprehensive total power modelling of a multirotor.

$$\mathbf{P_i} = \mathbf{T}\boldsymbol{\nu} \tag{3.7}$$

3.2 Optimisation

Battery-powered UAVs are subject to limited flight endurance, which is a function of the aircraft's travel speed [35, p. 104]. Unlike traditional winged aircraft, multirotors do not have enough wing surfaces to provide a lift phenomenon (as fixed-wings do), and must therefore rely solely on propulsion for lift [12, p. 1424]. Thus continuously consuming energy to support their weight during flight. To address this challenge and achieve energy conservation, multirotors can employ two potential strategies:

1. Minimise power usage by moving at an optimal speed, such that the power consumption can be lowered, resulting in extended flight endurance. This approach focuses on finding an optimal balance between speed and power efficiency.

2. Minimise power usage per unit of speed in order to achieve the highest distance covered or task completed with the least amount of power consumed

In both cases, the relationship between speed and power consumption is important to consider. When a quadcopter needs to move at higher speeds, an increase in body inclination results in a loss of lift, necessitating additional propulsion effort to remain airborne [12, p. 1424]. Furthermore, during forward flight, power demands escalate as rotor torque must overcome parasitic drag, which becomes a significant and dominant resistance force at higher speeds. Therefore, it is essential to assess whether the energy saved from increased speed outweighs the additional energy required to counteract the loss of lift. Eventually, the choice of the optimal flying speed depends on whether the objective is to maximise airborne endurance or cover the maximum distance range.

To determine the optimal pitch angle for the optimum flying speed must be identified. The optimum flying speed for minimum total power loss is referred to as the speed that results in the least amount of drag [20, p. 179], where the total drag F_D consists of parasitic D_p, profile D_f and induced D_i drag as shown in equation (3.8) respectively. Thus, when the total drag F_D is at its minimum, the total power required P_{total} by the multirotor is also at its minimum.

$$F_D = D_p + D_f + D_i \tag{3.8}$$

3.2.1 Physics constraints

Since it is assumed the system has reached steady-state, $\dot{\boldsymbol{\nu}} = 0$. Subsequently, $\boldsymbol{\tau}$ from (2.15) in Subsection 2.3.2 must therefore satisfy equation (3.9). Thus, these physics-based constraints form an essential component of the optimisation problem formulation.

$$\begin{aligned} \dot{\boldsymbol{\nu}} &= 0 \\ \mathbf{M}^{-1}\Big(\boldsymbol{\tau} - \mathbf{C}(\boldsymbol{\nu})\boldsymbol{\nu}\Big) &= 0 \\ \Rightarrow \boldsymbol{\tau} - \mathbf{C}(\boldsymbol{\nu})\boldsymbol{\nu} &= 0 \\ \boldsymbol{\tau}_{\text{act}} - \boldsymbol{\tau}_{\text{G}} - \boldsymbol{\tau}_{\text{res}} - \mathbf{C}(\boldsymbol{\nu})\boldsymbol{\nu} &= 0 \end{aligned} \tag{3.9}$$

In addition to physics-based constraints, regulatory constraints will also be taken into account in the optimisation problem. However, due to the great variation of regulatory requirements from different cases, these will instead be discussed later in Chapter 7 for each individual case study.

3.2.2 Optimisation problems

Optimum flying speed for maximum flight time

The optimisation problem can be formulated as a nonlinear programming problem on the form shown in (3.10).

$$\begin{aligned} \min \quad & P_{\text{total}}(v) \\ \text{s.t.} \quad & \text{Physics constraints:} \\ & \boldsymbol{\tau}_{\text{act}} - \boldsymbol{\tau}_{\text{G}} - \boldsymbol{\tau}_{\text{res}} - \mathbf{C}(\boldsymbol{\nu})\boldsymbol{\nu} = 0 \\ & \text{Regulatory constraints:} \\ & 0 \leq V_{\text{ix}} \leq V_{\max} \end{aligned} \tag{3.10}$$

Optimum flying speed for maximum range

It is assumed the simplification in (3.11) can be applied to the optimisation problem.

$$\begin{aligned} E &= Pt \\ \frac{E}{s} &= \frac{P}{v} \end{aligned} \tag{3.11}$$

Then the optimisation problem can be formulated as displayed in (3.12) respectively.

$$\begin{aligned} \min \quad & \frac{P_{\text{total}}(v)}{v} \\ \text{s.t.} \quad & \text{Physics constraints:} \\ & \boldsymbol{\tau}_{\text{act}} - \boldsymbol{\tau}_{\text{G}} - \boldsymbol{\tau}_{\text{res}} - \mathbf{C}(\boldsymbol{\nu})\boldsymbol{\nu} = 0 \\ & \text{Regulatory constraints:} \\ & 0 \leq V_{\text{ix}} \leq V_{\max} \end{aligned} \tag{3.12}$$

3.2.3 Implementation of optimisation problems

All computational work was conducted on a 16-inch Macbook Pro with an Apple M2 MAX-chip with a 12-core CPU, 17-core GPU and 32 GB RAM running macOS Ventura 13.2.1. The optimisation process is implemented in Julia, a high-level programming language [41]. Moreover, the JuMP package [42] is utilised in conjunction with the IPOPT (Interior Point OPTimizer) solver [43] for solving the optimisation problem.

JuMP is a domain-specific modelling language used for mathematical optimisation, which is embedded in Julia. It supports a wide range of problem classes, including linear, mixed-integer, second-order conic, semidefinite, and nonlinear programming, and can be used for constrained optimisation problems for which formulate using the language of mathematical programming [44]. JuMP provides flexibility for both open-source and commercial solvers, including IPOPT. IPOPT is an open-source software package specifically designed for large-scale nonlinear optimisation problems [45], and is used to solve general nonlinear programming problems of the form:

$$\begin{aligned} \min_{x \in \mathbb{R}^n} \quad & f(x) \\ \text{s.t.} \quad & g^L \leq g(x) \leq g^U \\ & x^L \leq x \leq x^U \end{aligned} \tag{3.13}$$

Then the optimisation problems defined in Subsection 3.2.2 can be implemented in Julia. A brief overview of the process can be seen in Listing 3.1.

Example

In the following example, an initialisation set-up file is provided for each multirotor. The initialisation file contains crucial information such as weight, propeller radius, and battery energy. The code then utilises this information, along with data sheets or wind tunnel test results, to calculate the drag and thrust coefficients required for further computations.

Furthermore, the code defines variables and constraints relevant to the drone model, with different constraints assigned using @variable, @NLconstraint, or @constraint. Towards the end of the code, the cost function is specified to minimise the total power, and the problem is subsequently optimised. Finally, the code allows for reading and plotting of the resulting values.

Listing 3.1: Example of implementation of optimisation problem

```
using JuMP, Ipopt                  # JuMP and IPOPT
model = Model(Ipopt.Optimizer)     # model generated

## Simulation initialisation setup of multirotor
include("M300.jl")                 # M300 details

## Inflow setup
InflowModel.init                   # inflow model initialised

## Drone model variables and constraints
@variable(model, theta >= 0)       # Pitch angle
@NLconstraint(model, Vbx, Vbx == - cos(theta) * Vxi)
@NLconstraint(model, Vbz, Vbz == - sin(theta) * Vxi)

# More variables and constraints
[...]

## Regulatory constraints

## Power constraints
# Parasitic, profile and induced power constraints

# Cost function
@objective(model, Min, P_total) # Cost function created

# Solve the problem
optimize!(model)                   # Optimisation

# Values can be read and thus plotted
theta    = value.(theta)*180/pi    # optimal theta
Vix      = value.(Vxi)             # optimal forward speed
```

4 Regulations on aviation with unmanned aerial vehicles

The development of all aspects of the drone market has proceeded at a fast pace that has shown to be demanding to catch up with from a regulatory point of view. In Norway, drone regulations have been implemented since 2016 and it is still an ongoing work [6]. However, people have been flying drones both privately and professionally long before the implementation. DJI, SZ DJI Technology, the world's largest consumer drone manufacturer was already established in 2006 [46], and the famous DJI phantom model hit the market back in 2013 [3]. The (less) well-known models 3DR iris+ and FreeFly's CineStar for consumer and professional application date back to 2014 and 2011 respectively. Thus, BSL A 7 was a step towards professionalising the drone industry which up until 2016 was allowed to largely unfold on its own.

In this chapter, the regulations in Norway will first swiftly be accounted for. Afterwards, specific parts of the regulatory framework relevant to later chapters will be highlighted, namely civil state aviation and the specific category. The aim is to provide some insightful and relevant information about the regulatory framework in order to navigate through paragraphs and laws that still to this date are under constant development and revision.

Figure 4.1: The drones DJI Phantom 1 [3], 3DR iris+ [4] and CineStar 6 [5] where some of the models sold on the market long before BSL A 7 took effect

4.1 U-space

Although not directly relevant to the report, it is worth mentioning U-space as it contributes to a comprehensive overview of the ongoing efforts aimed at facilitating the future integration of UAs. From the perspective of the foreseen increase of drone traffic due to the scale-up volume of drone operations, safe operations and management of drone traffic are of importance. EASA has since 2017 been working on U-space which gradually will be implemented in Norway from 2023 [24].

The term U-space is used to describe the management of unmanned aircraft traffic in order to ensure safe interaction between entities that are using the same airspace [47]. Thus by introducing new services and procedures, such as air traffic management (ATM) information service, detect and avoid (DAA) system and geofencing for drones, the objective is to facilitate unmanned and manned aircrafts operating along each other [24].

Up until today, the number of drone flights across a wide range of applications has risen under an initial regulatory framework where small drone operators only have regulated access to the VLL airspace. Therefore, it will be essential for a safe and equitable integration of current and future operations, especially in more urban airspace where the density of traffic is larger and ground risk is expected to be higher [48, p. 2].

4.2 BSL A 7

On the 1st of January 2016 BSL A 7-1, Norway's first national regulation on unmanned air crafts took effect [6]. However, in 2021, BSL A 7-2 was added, which incorporated the EASA Regulations into Norwegian law, thereby extending the regulations established in 2016 [7]. BSL A 7-1 was then mainly reserved for civil state aviation [7]. The new regulations, specifically EU Regulations 2019/947, 2020/639, 2020/746, 2021/1166 and 2022/425, were then adopted in order to achieve a common European regulatory framework for the safe operation of civil drones. The purpose of the reform is to obtain a harmonised drone market, where operators are allowed to circulate freely in the EU once authorised by their country's NAA. Overall, the implementation of BSL A 7-2 will have significant financial and administrative consequences both for the CAA, manufacturers and drone operators, and certain consequences for consumers as well as other authorities [49].

BSL A 7 provides general restrictions and requirements applied to civil UAS operators. Thus regulations will encompass commercial and recreational purposes, as well as governmental. The regulations include but are not restricted to requirements associated with operators, air crafts and areas overflown. For instace, safety distances, weight- and speed limitations of aircraft, and OM adapted to the complexity of the undertaking's operations.

The regulations aim to ensure that operations are conducted in a considerate manner without risk of harm to people, animals or property by identifying and mitigating risk as well as increasing knowledge of personnel executing operations. It can also be mentioned BSL A 7 does not apply to the Norwegian Armed Forces' use of unmanned aircraft as well as military aviation within restricted or danger areas [50].

4.2.1 BSL A 7-2

Figure 4.2 provides a comprehensive overview of BSL A 7-2, which includes open, specific, and certified categories. The boxes with three dots represent upcoming categories that have not been released yet but are anticipated to be included in the near future. Given that professionals often carry out and plan more higher-risk operations, and therefore are more likely to operate within the specific drone category, this report will primarily focus on the specific category to provide relevant insights for operators encountering similar circumstances.

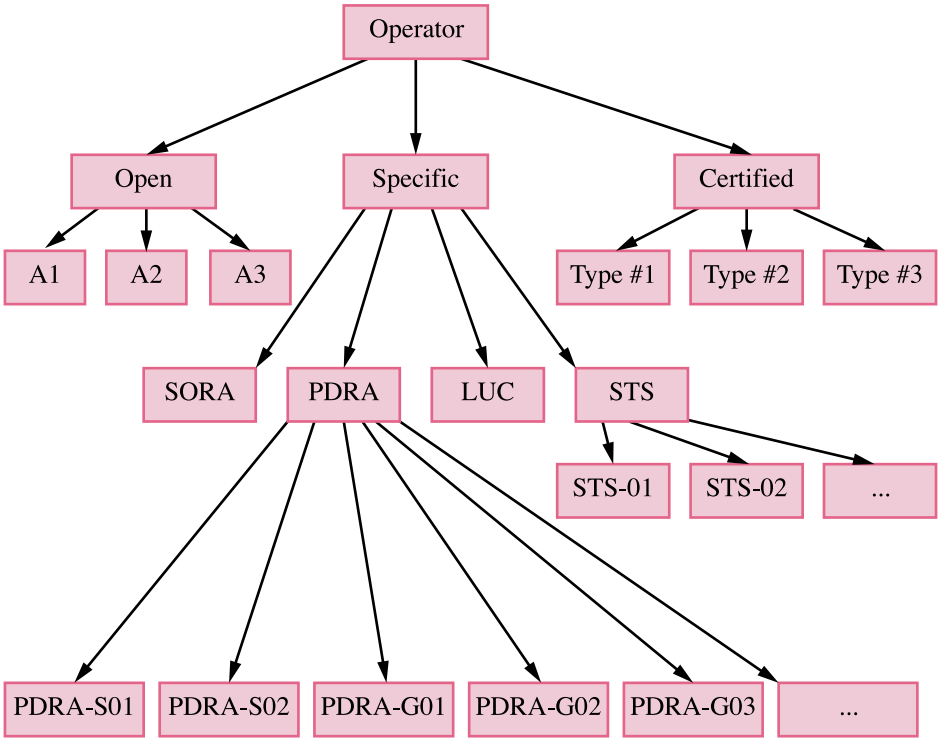

Figure 4.2: Total overview of categories and sub-categories of BSL A 7-2. The figure is composed based on information found in BSL A 7 [6, 7] and EASA's directory [8]

4.3 Specific category

As already depicted in figure 4.2, there are four different ways to operate in the specific category [51]:

- Obtaining an operational authorisation through Specific Operation Risk Assessment (SORA)
- Obtaining an operational authorisation following a Predefined Risk Assessment (PDRA), which eventually is a pre-made SORA developed by EASA for the drone operator
- Submitting a declaration based on a standard scenario (STS), but it necessitates the drone to possess a specific C-classification
- Have a Light UAS Operator Certificate (LUC), which grants the operator the authority to approve SORA, PDRA, or STS

It can be mentioned STS first is set to be applicable from the 1st January 2024, and thus not yet relevant [51]. LUC is on the other hand an operational certificate intended for experienced operators that allow them to obtain authorisation to approve their own operations [52]. Hence, the continuous focus in this report will only encompass the SORA methodology and PDRA.

4.3.1 SORA

SORA is a risk assessment methodology designed specifically for drone operations, proposed by the Joint Authorities for Rulemaking on Unmanned Systems (JARUS). It is essentially a ten-step process that assesses the risk of operations in a comprehensive and standardised manner. The aim is to identify potential safety risks associated with drone operations, evaluate identified risks and determine the acceptability of a proposed operation as well as develop appropriate measures in order to prevent possible accidents or injuries [53].

The SORA methodology involves a systematic approach to risk assessment, taking a wide range of factors into account, such as the operating environment, the drone characteristics, the competency of the pilot, and the potential impact of the operation on people, property, and other airspace users, in order to determine the boundaries required for a safe operation [53, 54]. By using a standardised approach to risk assessment, SORA provides a consistent and repeatable process for evaluating drone operations and ensuring that appropriate risk management measures are implemented. The ten-step SORA methodology can be briefly summarised as follow [32, 53, 54]:

1. **ConOps description:** Describes both the UAV and the operation

2. **Intrinsic ground risk class (GRC) determination:** The classification relates to the risk of a person being struck by the UAS. Thus based on the UAS characteristics dimension, expected typical kinetic energy and operation scenarios, a numerical value is indicated

3. **Final GRC determination:** The intrinsic risk can be reduced and modified by means of mitigation. Thus the final GRC determination is based on the availability of these mitigations to the operation and established by adding all the correction factors, namely M1, M2 and M3

4. **Initial air risk class (ARC) determination:** The initial assignment of airspace collision risks before mitigations are applied, and are specified with a letter from A to D

5. **Strategic mitigation for air risk:** Application of strategic mitigations to determine the residual ARC, but can only be applied if the UAS operational volume has a different collision risk than the one that the initial ARC would indicate

6. **Tactical mitigation of air risk:** The aim is to ensure that Tactical Mitigations Performance Requirements (TMPR) are satisfied. Mitigations are applied to mitigate any residual risk of a mid-air collision

7. **Specific Assurance and Integrity Level (SAIL) determination:** The SAIL value provides an overall assessment of the risk level and is determined by the final GRC and residual ARC, and represents the level of confidence that the UAS operation will remain under control

8. **Operational Safety Objectives (OSOs) determination:** The SAIL value is used to evaluate the defences within the operation in the form of 24 OSOs, and to determine the associated level of robustness. Then the OSOs define requirements for technical systems, training and procedures

9. **Adjacent area/airspace considerations:** The objective is to address the risk posed by a loss of control during an UAS operation that could result in infringement of adjacent areas on the ground or in the adjacent airspace.

10. **Comprehensive portfolio:** The safety portfolio usually consists of OM, ConOps, checklists etc.

4.3.2 PDRA

To avoid repetitive individual approvals for ConOps with known hazards and acceptable risk mitigations, EASA has applied the SORA methodology to define STSs and PDRAs [32, p. 42]. Thus, if an operation falls within the scope of one of the published PDRAs, it enables the applicant to swiftly develop the operator manual and the evidence of compliance using the PDRA table to demonstrate the safety of the operation [55].

As of now, five PDRAs have been published, namely PDRA-S01, PDRA-S02, PDRA-G01, PDRA-G02 and PDRA-G03. However, PDRA-05, PDRA-06, PDRA-07, and PDRA-08 are still undergoing evaluation by EASA, and have not yet been adopted by the Norwegian CAA [55]. The different PDRAs cater distinct operating scenarios, where each is clearly defined in scope and limitations [55, 56]. For instance, PDRA-G03 can be briefly described as follows:

- **PDRA-G03**: BVLOS flight over a sparsely populated area. Within radio range. Customised for line inspection, but can also be used for agricultural works. PDRA-G03 can only be issued for precisely defined areas.

4.4 Civil state aviation

According to § 69 in BSL A 7-1, civil state aviation is defined as police operations, customs operations, public search and rescue services, firefighting, coast and border guards or similar activities and services [6]. The operations are required to be of public law purpose character in order to be categorised as civil state aviation [57]. Other operations are subject to the general operating rules for drones in BSL A 7-2, regulations on aviation with unmanned aircraft in the open and in the specific category.

Civil state aviation is divided into three RO categories, each governed by its own set of rules and properties. Figure 4.3 offers an overview of the architecture, which appears to be simpler in comparison to BSL A 7-2. One of the shared requirements for all RO categories is the need to obtain an OM, which provide detailed information about the organisational structure, types of operations, and maintenance procedures, as well as risk analysis and assessment of the respective operations.

Table 4.1 highlights significant distinctions among the RO categories. To operate as a RO 1 operator, self-declaration and insurance coverage are adequate. However, both RO 2 and RO 3 operators require approval from the CAA. In terms of vertical and horizontal safety distances for RO 3, the exact distances can vary depending on the approved OM. The CAA will evaluate the sufficiency of safety measures and emergency plans to ensure compliance with the reduced safety distances.

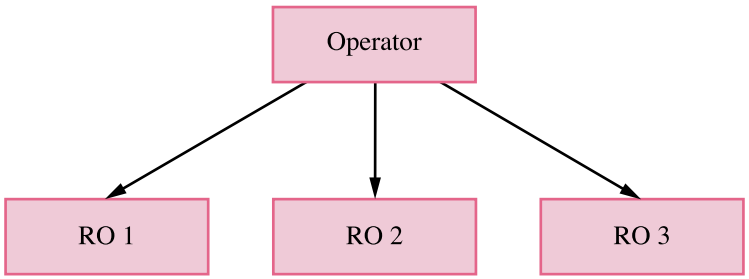

Figure 4.3: Civil state aviation

Table 4.1: Overview of certain different features between different RO categories

	RO 1	RO 2	RO 3
AGL	120 m	120 m	120 m but can also be more*
Safety distance to people, motor vehicles or building not under the pilot's and commander's control	50 m	50 m	50 m but can also be less*
Safety distances close to population of more than 100 people	150 m	150 m	150 m but can also be less*
MTOM	2,5 kg	25 kg	$>$ 25 kg
Maximum speed	60 knop $\approx$ 30 m/s	80 knop $\approx$ 41 m/s	$>$ 80 knop or powered by a turbine engine
Types of operation	VLOS	VLOS, EVLOS and BLOS	VLOS, EVLOS and BLOS
Light	Daylight	Any	Any

5 Case studies

Optimising the energy consumption of drones can be socially beneficial in several operational scenarios. Some examples could include:

- Infrastructure inspection of power lines, railway tracks, bridges or buildings
- Monitoring of agriculture or livestock
- Search and rescue (SAR) missing persons i.e. after a natural disaster
- Transportation of goods, for instance, medicine between hospitals, food to households as well other packages
- Give situational awareness in order to search and identify the source of for example gas leakage, fire, people who've fallen into the ocean or alternatively lost in the woods

In the upcoming sections, four distinct case studies will be presented, each examining different aspects of BSL A 7. The aim of these case studies is to assess whether the limitations outlined in the legislation have the potential to restrict the optimisation problem in certain operating scenarios. The objective is to offer insights that drone operators can consider or potentially incorporate into their procedures. Through the analysis of these scenarios, potential constraints within the current regulatory framework that may affect the efficient energy operation of drones can be identified.

The following case studies have been strategically selected to showcase various operation scenarios for different purposes:

1. State aviation, in particular, police
2. State aviation, SAR
3. Power line inspection
4. Filming in close proximity to crowds

The first case study will examine drone police missions during large events in state aviation, while the second case is an avalanche SAR scenario carried out by either state aviation instance. The third will address power line inspections using PDRA methodology, and the fourth will focus on close proximity filming using the SORA framework. The case studies presented in this report are intended to provide a general overview and insight into real-life drone operations. While the scenarios may be simplified for the purpose of discussion, they nevertheless serve as illustrative examples of drone applications in different operational contexts.

It is important to recognise that regulatory constraints for drone operations may not apply universally. While PDRA and RO 2 entail more stringent requirements, such as a maximum altitude or fixed speed limit, the SORA framework serves as a guiding framework for conducting drone operations. Consequently, the specific conditions approved for each operator will depend on the risk assessment and mitigation measures outlined in the OM, where each drone operator is responsible for demonstrating their capabilities within the regulatory framework to the CAA.

5.1 Case study: Police mission during larger events

The introduction of drones into police fieldwork in four police districts in Norway was carried out through pilot projects that began in 2019. Today drones are utilised by the Norwegian police for various operational missions, preparation for major events, SAR operations, and crime scene photography [58].

For large events, such as festivals and sporting events [59], the police use drones to gain an overview of gatherings of people to ensure people's safety, as well as monitor and record specific incidents when it is proportionate and necessary [60]. Drones are also employed in situations where they search for missing individuals who may have become lost in forests, ended up in the sea, or found themselves on the outskirts of events [59].

5.1.1 Drone specifications

Dji Matrice 300 RTK (M300), as shown in figure 5.1, is one of the drones commonly utilised by the police in Norway [61]. It has also been adopted by multiple fire departments for tasks such as monitoring wildfires, assessing damage from fires, and locating individuals who require rescue [62, 63]. Therefore, it can be argued that this drone model is frequently selected for performing state aviation tasks. A summary of the relevant specifications for the M300, obtained from the manufacturer's data sheet [64, 65, 66], is provided in Table 5.1.

Figure 5.1: Dji Matrice 300 RTK [9]

Table 5.1: DJI Mavic Matrice 300 RTK specifications

Aircraft body	**Value**
Dimensions L × W × H (propellers excluded)	810 × 670 × 430 mm
Diagonal wheelbase	895 mm
Weight	3.6 kg (with single downward gimbal excluding batteries)
	Approximately 6.3 kg (with single downward gimbal and dual TB60 batteries)
Max speed	23 m/s (S mode)
	17 m/s (P mode)
Max flight time	55 min (7 m/s without payload)
Propellers: 2110	**Value**
Unfolded diameter	53 cm
Battery: TB60	**Value**
Capacity	5935 mAh
Energy	274 Wh

5.1.2 Mission during larger events

The utilisation of quadcopters offers an aerial perspective that can aid in situational awareness and facilitate ground staff investigations. A prevalent aerial search technique involves hovering over specific vantage points, which offers a bird's-eye view of the surrounding area. This approach can prove particularly advantageous in scenarios where locating missing persons or identifying stranded individuals in difficult terrain or inaccessible areas is necessary.

Furthermore, quadcopters are capable of flying between various vantage points to capture a more comprehensive view of the area. This feature can be especially beneficial in circumstances where ground access is restricted or hazardous. An example of such a scenario can be observed in Figure 5.2, which depicts a festival area in close proximity to the sea, where circles indicate hovering vantage points and dotted lines routes between the respective points. In this setting, vantage points can be utilised to monitor both the water and the streets, ensuring comprehensive coverage of the vicinity.

- Hover on station: Monitoring people on the outskirts of the crowds by hovering over low population density areas and pointing IR-camera and photo-camera in different directions

- Flight: Searching for missing people on the outskirts of the crowds by flying to nearby locations such as the sea, rooftops or side curbs in an alley

5.1.3 RO 3

From Table 4.1 in Subsection 4.3.1, it becomes apparent operations involving drones for civil state aviation purposes often will either require RO 2 or RO 3 approval either due to the daylight requirement or MTOM. It can be noted the term night is defined as when the centre of the sun is 6° below the horizon [67]. Then it will for instance almost be impossible to operate during daylight during polar night in the northern part of Norway.

In light of the fact that RO 3 limitations are contingent upon the outcomes of individual risk assessments, which may vary significantly between operators, a proposal which differs from RO 2 will be given. As such, the optimisation problem for this particular case be constrained by the following suggested conditions [6]:

- A maximum altitude of 100 meters above ground level (AGL)

- A minimum ground risk buffer of 50 meters from populations consisting of more than 100 individuals

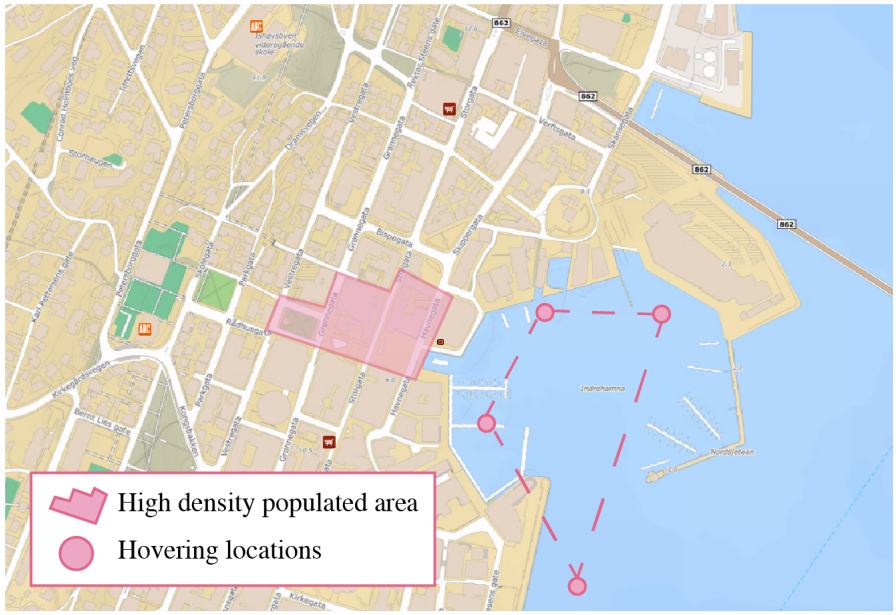

Figure 5.2: High-density populated area with four hovering locations marked with circles, and dotted lines representing routes to get another angle of the situation

5.2 Case study: SAR mission conducting a surface search operation in the sea

Drones have proven to be invaluable tools in SAR missions because of their ability to efficiently cover large areas, reach inaccessible locations, and provide rescuers with real-time data. However, drones can so far not replace other resources on the ground during SAR operations but rather complement them. For instance, in areas characterised by dense vegetation, ground crews remain indispensable and a critical component. Similarly, in the aftermath of an avalanche, helicopters continue to play a vital role due to their superior response time, specialised transmitter/receiver equipment, and capacity to efficiently transport individuals when necessary.

SAR drones are equipped with various sensors, including Electro-Optical/Infra-Red (EO/IR) cameras (that include both visible and infrared sensors), which can provide valuable information to rescuers to locate and assess the situation of people in distress. Effective use of SAR drones requires knowledge of SAR techniques, such as search patterns and communication with other rescue personnel. Additionally, operators must possess the necessary skills and familiarity with established routines to operate the equipment proficiently and to ensure that it is used correctly and effectively in the given situation.

The Joint Rescue Coordination Centre (JRCC) generally holds overall responsibility for coordinating and summoning resources for a search and rescue mission until the Local Rescue Centre assumes control [68]. At the local level, the incident manager is tasked with making informed decisions and overseeing the operation. This includes coordinating the drone operation and defining the search pattern based on observations of the conditions and terrain. It is customary to rely on the nearest available resource, such as the police, Coast Guard, the Red Cross, or Norwegian People's Aid, to respond to the mission under the given circumstances.

5.2.1 Drone specifications

For the sake of simplicity, the use of M300 will be continued as it is a widely adopted model by state aviation operators and a frequently used model by other organisations as well. The specifications are thus summarised in Table 5.1 in Subsection 5.1.1.

5.2.2 Search flying patterns

Various visual search patterns exist for SAR missions, such as sector search, expanding square search, track line search, and parallel sweep search (PS) [69, p. 5-6]. The selection of the search pattern depends on factors specific to the mission, such as the size of the search area, weather conditions, and available resources. An essential factor to consider is whether there is any information regarding the scope of the search, whether it is a fine or rough search.

For certain SAR missions conducted with airborne vehicles, such as those involving drones or helicopters, the PS search pattern is particularly effective for providing uniform coverage of a large area when uncertainty in the survivor's location is large [69, p. 5-9]. Therefore, variations of parallel search patterns are often chosen in cases when conducting a surface search operation in the sea, namely pattern 1 (P1), pattern 2 (P2) and pattern 4 (P4). These patterns are illustrated in Figures 5.3, 5.4, and 5.5, respectively. A standard for the M300 involves flying all patterns with the H20T gimbal angle set to 75° and a search height of 100 m AGL.

P1 is mainly utilised in open terrain and can be executed rapidly, although its accuracy is usually low to medium. P2 is suited for larger areas with varying vegetation but takes longer and depends on the search area's size for completion. The accuracy of P2 ranges from medium to high, depending on vegetation density. P3 is a meticulous search and requires much more time to complete than the other patterns.

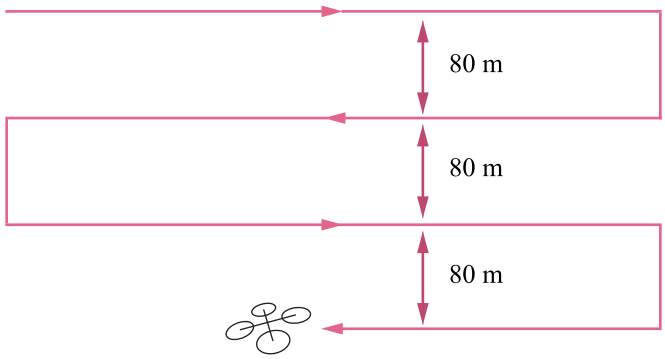

Figure 5.3: P1: Parallell sweep search

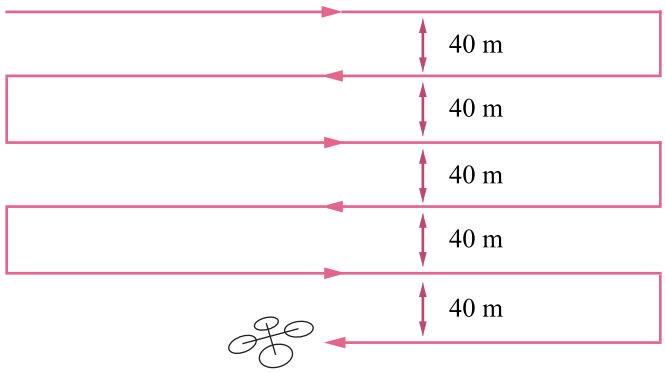

Figure 5.4: P2: Parallel search with overlap

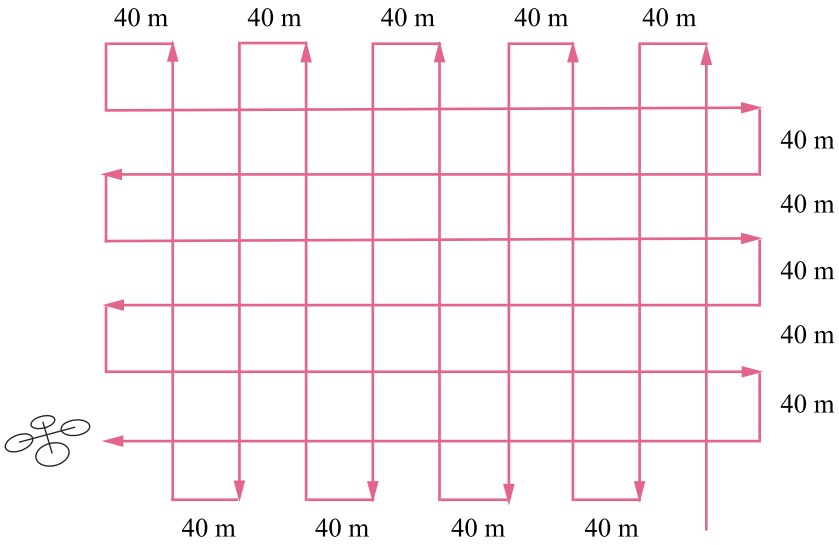

Figure 5.5: P4: Parallel pattern crossing with overlap

5.2.3 RO 2

Surface search operations in the sea for SAR missions are typically conducted in areas with low population density and can therefore classify as RO 2 operations. Although the maximum allowable flight height is 120 m, the common practice is to set it at 100 m AGL. This is likely due to extended air space segregation and improved ground view coverage. Consequently, the following operating conditions are listed [6]:

- Max 100 m AGL
- Min 150 m safety distance to a population of more than 100 people
- Max speed 41 m/s

5.3 Case Study: Commercial entity conducting BVLOS power line inspections in sparsely populated area

The inspection and maintenance of power lines are critical in order to ensure the safe and continuous distribution of electricity. Any damage or fault in the lines may lead to serious safety hazards for both people and property. Thus the inspection can help identify these hazards as well as prevent accidents as the lines are subject to degradation.

Inspection of high-voltage power transmission lines has traditionally been carried out by manned aerial vehicles or foot patrol. However, these maintenance methodologies are inefficient and expensive compared to drones, which have emerged as a popular tool for conducting power line inspections instead. UAVs represent an alternative to manned systems, both reducing the risk to personnel involved as well as cutting costs, for a wide range of activities related to monitoring transmission lines as well as other types of strategic infrastructure [70, p. 1].

5.3.1 Drone specifications

For manual inspection of single wiring masts, a small drone such as DJI Mavic 3 can be used for a brief examination. However, for autonomous inspection, M300 is more useful because of its advantageous power capacity and will therefore be served in this case. The details are already summarised in Table 5.1 in the previous section.

5.3.2 Normal flight procedures

During a power line inspection using a quadcopter, it is common to equip the drone with a combination of different sensors, including cameras, LIDAR, and/or IR cameras. The quadcopter is flown along the power lines and captures images and data for inspection, which potentially can help identify corrosion, damage or vegetation encroachment. The flight path will typically follow the trajectory of the power lines, where forward flying constitutes the largest part of the flight operation compared to hovering.

For simplicity, two key procedures that can be identified during a power line inspection are as follows:

- Hover over poles in order to inspect specific details or discrepancies on power poles
- Maximising the distance of lines covered by the drone using the available power

5.3.3 PDRA-G03

PDRA-G03 is specifically designed for linear inspections, and has been documented by EASA [32, p. 136]. As a result, it can be used as a simplified alternative to developing a SORA, which is why it was utilised in this case study. Furthermore, it can also be used as a basis for future assessments if desired.

A selection of operational preliminaries for the PDRA-G03 is condensed into Table 5.2, which details will be taken into account. A full overview of the operating scope as well as more detailed requirements are provided by the Norwegian CAA on their respective website [56].

In Figure 5.6 two different scenarios are defined, where the height of the power pole either has a height (a) up to 20 m or (b) higher. Thus the height at which the drone can fly from the top of the pole being inspected will vary depending on the height of the pole. It can also be noted the operational volume requires the contingency volume to be at least 20 m taller than the flight geography.

Table 5.2: PDRA-G03

Condition	
Maximum characteristic dimensions (maximum distance between rotors)	3 m
Max typical kinetic energy	34 kJ
Maximum flight geography	30 m AGL
(a) Maximum distances when operating in the proximity of natural or artificial obstacles (e.g. trees, buildings, towers, cranes, fences, etc.) whose height is below 20 m	30 m horizontally and 30 m vertically from the top of the overflown. The maximum flight geography height is 50 m
(b) Maximum distances when operating in the proximity of natural or artificial obstacles (e.g. trees, buildings, towers, cranes, fences, etc.) whose height is above 20 m	30 m horizontally and 15 m vertically from the top of the overflown obstacle
Contingency volume	Minimum 20 m taller than the flight geography
Ground risk buffer	Default criterion: 1:1 rule

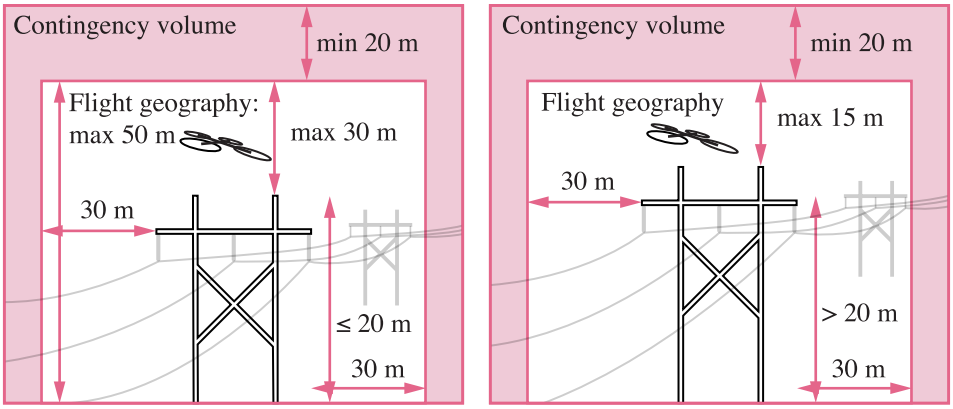

(a) If the obstacle height does not exceed 20 m, the height of the operation may be up to 30 m from the top of the obstacle. The maximum operating height is 50 m AGL. The maximum horizontal distance from the obstacle is 30 m

(b) If the obstacle height is taller than 20 m, then the height of the operation may be up to 15 m from the top of the overflown obstacle. The maximum horizontal distance from the obstacle is set to 30 m

Figure 5.6: Safety distances in order to decrease air risk according to PDRA-G03

5.3.4 Typical kinetic energy

Although not explicitly included in the cost function, there are certain requirements related to the typical kinetic energy that must be fulfilled. To estimate the energy possessed by a drone upon impact with the ground, the typical kinetic energy is computed using the equation (5.1), where the net force F is the difference between drag F_D and weight F_G.

$$F = F_D - F_G \tag{5.1}$$

When F_D is equal to F_G, there is no net force [71]. By inserting the drag equation (2.3) into (5.1), equation (5.2) is obtained.

$$\begin{aligned} F_D &= F_G \\ \frac{1}{2}\rho A C_D v^2 &= F_G \end{aligned} \tag{5.2}$$

Terminal velocity v_T is then calculated as in (5.3) [71].

$$\begin{aligned} v_T &= \sqrt{\frac{2F_G}{\rho A C_D}} \\ &= \sqrt{\frac{2mg}{\rho A C_D}} \end{aligned} \tag{5.3}$$

Thus the total typical kinetic energy tke can be estimated in (5.4).

$$tke = \frac{1}{2}mv_T^2 \tag{5.4}$$

To comply with the legal regulations, it is necessary to ensure that tke remains below 34 kJ. This restriction imposes limitations on the selection of drones suitable for the mission, including factors such as weight F_G and size, which directly influence the frontal area A of the drone.

5.3.5 Maximum horizontal speed

The horizontal distance that the quadcopter travels between the moment of failure and hitting the ground can be calculated according to [72, p. 2], where air resistance in the horizontal axis will be taken into account.

First, β is defined as (5.5), which originates from drag equation in (2.3) [73, p. 8].

$$\beta = \frac{\rho A C_D}{2m} \tag{5.5}$$

The vertical velocity v of an object that has fallen from a height h is given by equation (5.6) respectively.

$$v^2 = \frac{g}{\beta}(1 - e^{-2h\beta}) \tag{5.6}$$

Given the vertical velocity v, the elapsed time t between the moment of failure and impact is given in (5.7) [72, p. 3].

$$t = -\frac{1}{4\sqrt{\beta g}} ln(\frac{(v\sqrt{B} - \sqrt{g})^2}{(v\sqrt{\beta} + \sqrt{g})^2}) \tag{5.7}$$

The distance x is the minimum ground risk buffer, which as the default criteria should be according to the 1:1 rule. Then the horizontal velocity at the time of failure is given by v_{max} in equation (5.8).

$$v_{max} = \frac{x}{t} \tag{5.8}$$

This can further be implemented as constraints in the optimisation problem. For the calculation of the cross-sectional area A, this can for instance be done according to [72, p. 3]. Although the calculation is not accurate, it gives an estimate.

5.4 Case study: Filming in close proximity to a high density of people (crowds) in an urban environment

Drones have become an increasingly popular tool for capturing aerial footage in a variety of industries, allowing professionals to capture angles that were previously impossible to achieve. As a result, a wide range of professions, such as film creators, news organisations, sporting events, as well as event planners and real estate agents, can benefit from using drones.

However, filming in close proximity to crowds also imposes increased risks. Therefore, if high photo resolution is essential for the project, SORA may be a better option than the open category as it allows for the additional weight of larger cameras. Nevertheless, this may require drones with greater lifting capacity, which can amplify the consequences in case of a drone crash. The next section will outline an operational scenario, but the principles and guidelines can also be applicable to executing drone operations in various contexts.

5.4.1 Drone specifications

The DJI Inspire 2 (I2) has been a popular tool in the aerial photography industry due to its RAW image quality, compact size, and competitive price point. In this case study, the latest addition in line, DJI Inspire 3 (I3) seen in Figure 5.7, which was released to the global market in June 2023 will be the focus. Data sheet specifications provided by the manufacturer of the aerial cinematography drone are summarised in Table 5.3 [10].

Figure 5.7: Dji Inspire 3 [10]

Table 5.3: DJI Inspire 3 specifications

Aircraft body: T740	**Value**
Dimensions L × W × H (propellers excluded)	425mm × 427mm × 316 mm
Weight (includes gimbal camera, two batteries, lens, PROSSD, and propellers)	3.995 kg
Max horizontal speed	26 m/s
Max hovering time (with landing gear raised)	Approx. 25 minutes (with gimbal camera and lens)
Max flight time (10 m/s)	Approx. 26 minutes (landing gear raised)
	Approx. 28 minutes (landing gear lowered)
Propellers: 1671 quick-release	**Value**
Diameter	40.6 cm
Battery: TB51	**Value**
Weight	0.470 kg
Capacity	4280 mAh
Energy	98.8 Wh

5.4.2 Normal flight procedures

During drone operations, the drone may not always fly continuously in a forward direction. However, in order to simulate, some generalisations are necessary. Similar to the previous case studies, the following manoeuvres can be identified:

- When waiting for a scene to unfold, maximising flight time can be useful. In single-camera productions, there may be some waiting time on the subject, while in multi-camera productions, camera operators may need to queue up, making it advantageous to stay airborne for as long as possible to avoid missing any shots or incidents. On a film set, time is considered everything
- It is normal to take advantage of all the camera axes in flight, but some very common movements are dolly zooms and panorama shots, which often only require movement in surge or sway (in addition to some camera movement)

5.4.3 SORA

It is assumed that the following conditions can be achieved through a thorough SORA process, making it applicable to represent a realistic operational scenario. The necessary actions to fulfil the final GRC, residual air risk, SAIL, and OSOs should be implemented in the OM. Table 5.4 briefly summarises the results of the risk assessment with mitigations.

Table 5.4: Main features and assumed final risk values for SORA

Operation type	VLOS
Area	Urban
Height	Maximum 120 m

Inherent ground risk				4
Mitigation	M1 = -1	M2 = 0	M3 = 0	-1
Final ground risk (GRC)				3

Initial air risk	ARC-C
Residual air risk	ARC-B

SAIL	II

The detailed documents to support the SORA are the OM, ConOps as well as a contingency plan and emergency plan in the occurrence of accidents and incidents. However, it is not normal procedure to enclose these documents as they are considered proprietary information and trade secrets that are critical to a company's operations and competitive advantage. Nevertheless, it should be possible to attain similar results through the ten-step SORA process previously described in Subsection 4.3.1.

Two different horizontal proximity limits, 50 m and 25 m, are listed with accompanying operation limits. These could later potentially constrain the optimisation problem, and is shown in Table 5.5 and 5.6 and illustrated in Figure 5.8 and 5.9, respectively. The maximum horizontal speed is determined based on the calculations outlined by Shelley in mind [72, p. 2], which already is described in detail in Subsection 5.3.5.

Table 5.5: Horizonal proximity: 50 m

Height	Max horizontal speed
25 m	15 m/s
50 m	9.5 m/s
80 m	6.5 m/s
120 m	4.5 m/s

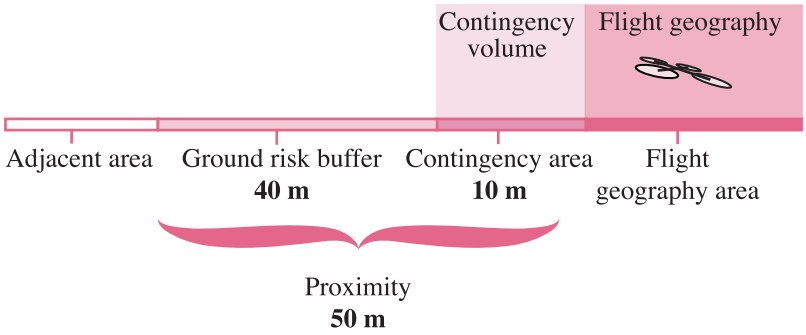

Figure 5.8: Horizontal proximity of 50 m

Table 5.6: Horizonal proximity: 25 m

Height	Max horizontal speed
25 m	7.5 m/s
50 m	4.5 m/s
80 m	3 m/s
120 m	2.5 m/s

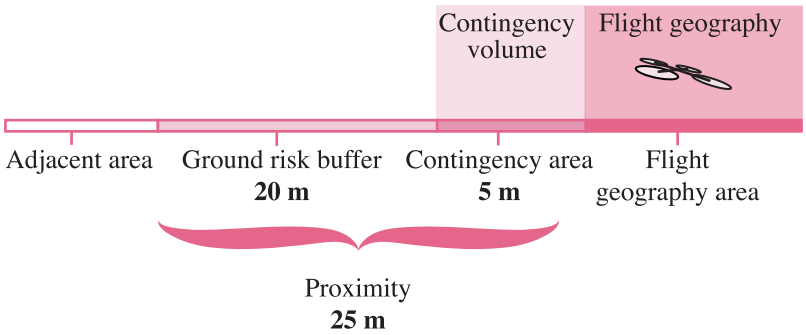

Figure 5.9: Horizontal proximity of 25 m

5.5 Implementation of operation types

Listing 5.1 provides a condensed representation of the regulatory constraints associated with the different types of drone operations listed in the previous sections. These constraints specify the maximum allowable values for the horizontal speed in the x-direction within the inertial frame, which may vary depending on the specific operation type.

To ensure compliance with regulatory requirements, it is essential to incorporate these constraints into Listing 3.1 of Subsection 3.2.3, which shows an overview of the implementation of the optimisation problem. By including the regulatory constraints as part of the ”model” variable, these constraints become an integrated component of the objective function, which allows for optimisation.

Listing 5.1: Types of operations implemented as constraints

```
##### Regulatory constraints #####

## RO 3
h = 100          # height AGL
d = 50           # horizontal distance
Cd               # drag coefficient
S                # cross section area

RO3_v_max = max_speed(h, d, Cd, S)       # function max v
@variable(model, 0 <= Vxi <= RO3_v_max) # constraint

## RO 2
RO2_v_max = knots_to_ms(80)              # conversion
@variable(model, 0 <= Vxi <= RO2_v_max) # constraint

## PDRA-G03
tke_max = 34000 # max typical kinetic energy
h = 50           # height AGL
d = 50           # horizontal distance
Cd               # drag coefficient
S                # cross section area

v_max = max_speed(h, d, Cd, S)           # function max v
@variable(model, 0 <= Vxi <= v_max)      #constraint

```

```
## SORA: urban
heights      = [25, 50, 80, 120]          # AGL
v_max_50m    = [15, 9.5, 6.5, 4.5]        # proximity 50 m
v_max_25m    = [7.5, 4.5, 3, 2.5]         # proximity 25 m
v_max_50m_25m = [v_max_50m, v_max_25m]    # max v values

for i in 1:length(v_max_50m_25m)
    v_max = v_max_50m_25m[i]              # max v
end

@variable(model, 0 <= Vxi <= v_max)       # constraint

## No operation type
@variable(model, Vxi >= 0)                # no constraint
```

6 Parameter identification and model validation

Model accuracy greatly depends on assigning accurate parameter values. These values can be determined either using data sheets or experimental data from wind tunnel experiments. Once identified, the model must be validated to ensure accurate predictions of system behaviour. This chapter will provide a detailed account of the techniques employed for parameter identification, along with the underlying assumptions. Furthermore, the chapter will delve into the validation of the model.

6.1 Calculation of parameters

6.1.1 M300 with DJI data sheet

The M300 drone by DJI is equipped with four DJI 6009 motors and 2110 propellers [64]. Characteristics for M300 are thus summarised in Table 6.1 and are essential in determining the appropriate simulation parameters.

Table 6.1: Additional M300 specifications

Parameter	Value
Hover power	175 W
Max power (full capability)	1000 W
Hover rotation speed (average)	2685 RPM
Max rotation speed (full capability)	5489 RPM

Thrust estimation

The thrust exerted during hover can be calculated as in equation (6.1), where m is the mass of the M300 drone and g is the gravity. This result can be then used to yield the thrust coefficient later on.

$$T_{\text{hover}} = m \cdot g \tag{6.1}$$

Power estimation

In hover, the total drag experienced by the multirotor is the combination of profile and induced drag [17]. In this state, parasite power loss is absent. Therefore, it is reasonable to assume that the total hover power P_{hover}, as provided in Table 6.1, can be expressed as the sum of profile power P_i and induced power P_f. This relationship is represented in equation (6.2).

$$P_{\text{hover}} = P_i + P_f \tag{6.2}$$

Further, momentum theory relates the rotor thrust and the induced velocity at the rotor disk by equation 6.3 [19, p. 31].

$$T = 2\rho A v^2 \tag{6.3}$$

Induced velocity in hover v_h is therefore (6.4).

$$v_h = \sqrt{\frac{T}{2\rho A}} \tag{6.4}$$

Thus the induced power loss for hover follows as in (6.5) when (6.4) is inserted [19, p. 31].

$$\begin{aligned} P_i &= Tv \\ &= 2\rho A v_h^3 \\ &= 2\rho A \left(\frac{T}{2\rho A}\right)^{\frac{3}{2}} \end{aligned} \tag{6.5}$$

Then equation (6.2) can be utilised to calculate P_f as in (6.6) in order to obtain the profile drag coefficient.

$$P_f = P_{\text{hover}} - P_i = k_d \omega^3 \tag{6.6}$$

Approximation of profile thrust coefficient

According to Nguyen, Liu and Mori [74, p. 36], the thrust coefficient C_T of a quadcopter is the average value of four rotors, as shown in (6.7).

$$C_T = \frac{1}{4}\sum_{i=1}^{4} C_{T_i} \tag{6.7}$$

Equation (6.8) shows the theoretical thrust T_{hover} during hovering, where ρ is the air density, A is the area of the propeller, ω is the angular velocity, and R is the propeller's radius.

$$\begin{aligned} T_{\text{hover}} &= C_T \rho A (\omega R)^2 \\ &= C_T \rho A R^2 \omega^2 = k_T \omega^2 \end{aligned} \tag{6.8}$$

From equation (6.8), k_T can be calculated as follows in (6.9).

$$k_T = \frac{T_{\text{hover}}}{\omega^2} \tag{6.9}$$

Then C_T can be obtained as a dimensionless constant in (6.10).

$$C_T = \frac{k_T}{\rho A R^2} \tag{6.10}$$

The thrust coefficient, C_T, is known to vary depending on the angle of attack, angular velocity, and other factors. In addition, during forward flight, the interference of multiple rotor configurations can also affect C_T. According to [74, p. 39], the thrust coefficient of the rear rotor is lower than that of the front rotor by a maximum of 11 %, which can degrade hovering performance. However, for the purposes of this report, the thrust coefficient will be treated as a constant value for simplicity.

Approximation of profile drag coefficient

From (6.6), k_D can be found in (6.11). The motor efficiency constant ε is added as well. A constant of $\varepsilon = 0.883$ is used for data sheets unless specified otherwise [75].

$$k_D = \frac{P_f}{\omega^3} \approx \varepsilon \frac{P_f}{\omega^3} \tag{6.11}$$

The dimensionless profile drag coefficient C_D defined in (3.5) can then be calculated in equation (6.12).

$$
\begin{aligned}
P_f = \frac{1}{2}\rho A C_D \omega^3 \quad \vee \quad P_f = k_D \omega^3 \\
\frac{1}{2}\rho A C_D = k_D \\
C_D = \frac{2k_D}{\rho A}
\end{aligned}
\tag{6.12}
$$

6.1.2 I3 with DJI data sheet

To protect trade secrets, DJI did not want to disclose all characteristics related to I3 or the DJI 3511s motor. As a result, the details were limited [10]. Therefore, the hover rotation speed (average) is provided by Mejzlík propellers instead, which provides a wide database of different propulsion systems in order make a baseline for further development and customisation [76]. The data from Mejzlík are marked with an asterisk (*) and is thus an approximation based on DJI 1671 propeller size and pitch. Table 6.2 thus provides an overview of the available information that will be used.

Since parameters were obtained through a data sheet similar to M300, identification was conducted by following the same method already stated in the previous subsection.

Table 6.2: 3511s and Mejzlík propeller specifications

Parameter	Value
Hover power	119 W
Hover rotation speed (average)	3089 RPM*
Max rotation speed (full capability)	7100 RPM

6.1.3 NASA wind tunnel test measurements

National Aeronautics and Space Administration (NASA) published 2018 wind tunnel and hover performance test results for a few selected multicopter vehicles, namely 3DR solo, DJI Phantom 3 (P3), 3DR Iris+, Drone America x8 and SUI Endurance. Characteristics from NASA's Phantom 3 test setup are collected in Table 6.3 [77, p. 3, p. 11], as well as additional details from the DJI datasheet [78], marked with (*), have been included to provide a more comprehensive overview.

Thrust coefficient

The thrust coefficient k_T and dimensionless version c_T were calculated as previously and defined in equation (6.13).

Table 6.3: P3 test characteristics

DJI Phantom 3	**Value**
Weight	2.8 lb
Dimensions L × W × H (excluding propellers)	9.9 in × 9.8 in × 7.6 in
Factory prop propeller diameter	23.88 cm
Baseline RPM	5300 RPM
Torque	0.398 in-lb
Max speed	16 m/s *
Max flight time (hover)	Approx. 25 minutes *

$$\begin{aligned} k_T &= \frac{T}{\omega^2} \\ c_T &= \frac{k_T}{\rho A R^2} \end{aligned} \tag{6.13}$$

Estimation of profile drag coefficient

Since the test data from NASA includes data for the torque τ in the z-direction, these measurements can be used to calculate k_D (6.14)

$$\begin{aligned} \tau &= k_D \omega^2 \\ k_D &= \frac{\tau}{\omega^2} \end{aligned} \tag{6.14}$$

Moreover, the dimensionless profile drag coefficient C_D can be obtained utilising the drag equation (2.3) as seen in (6.15) and (6.16).

$$\begin{aligned} F_D &= \frac{1}{2}\rho A C_D \omega^2 \\ \frac{\tau}{R} &= \frac{1}{2}\rho A C_D \omega^2 \\ \tau &= \frac{1}{2}\rho A C_D R \omega^2 \end{aligned} \tag{6.15}$$

$$\begin{aligned} \tau = \frac{1}{2}\rho A R C_D \omega^2 \quad \vee \quad \tau = k_D \omega^2 \\ \frac{1}{2}\rho A R C_D = k_D \\ C_D = \frac{2k_D}{\rho A R} \end{aligned} \tag{6.16}$$

6.1.4 I2 Xoar data

Lastly, performance data collected from a closed lab environment from the American propeller manufacturer Xoar Propellers will be listed, which was carried out using I2 combined with their carbon propellers [79]. Though I2 is similar to I3, it is simulated without camera equipment and a gimbal as another battery in order to replicate Xoar's conditions. Specifications for the drone and propellers can be briefly listed in Table 6.4. Additional information from DJI is included, marked with (*), that can be used to discuss and validate the simulation result [80].

Similar to the NASA tunnel data, information on thrust, torque and RPM is available. Therefore, the parameters can be calculated in a similar manner conducted in the previous subsection.

Table 6.4: I2 specifications

I2	**Value**
Weight	3.440 kg
Dimensions L × W × H (excluding propellers)	425mm × 427mm × 316 mm
Xoar propeller diameter	15”
Hover RPM	3559 RPM
Torque	0.155 Nm
Max speed	26 m/s *
Max flight time	Approx. 2* min (without camera) (hover) *
	Approx. 27 min (with Zenmuse X4S) (hover) *

6.2 Identified simulation parameters

Calculations from the previous section are summarised in Table 6.5. The obtained parameters are rounded to three significant figures for comparison, where k_T is the thrust constant, c_T is the dimensionless thrust coefficient, k_D is the drag constant, and c_D is the dimensionless profile drag coefficient.

Table 6.5: Identified simulation parameters

Drone	k_T	c_T	k_D	c_D
M300	1.95e-4	0.010	3.67e-6	2.72e-5
I3	9.36e-5	0.014	1.91e-6	2.40e-5
P3	1.10e-5	0.014	1.46e-7	4.46e-5
I2	6.35e-5	0.013	1.13e-6	8.51e-5

6.3 Validation of parameters

The study carried out by Nguyen, Liu and Mori [74, p. 36], shows the T-ω relationship when hovering for a quadcopter gives a k_T and c_T equal to 4.0e-5 and 0.013 respectively. However, for a forward flight, the study visualises how c_T might changes based on forward speed, RPM and AOA. There is a slight trend in the data that suggests c_T increases with forward speed while it decreases with increased RPM and AOA. The smallest value for c_T is thus given as 0.006 during a forward flight of 4 m/s at AOA -18° and 3000 RPM, whereas the largest is estimated to be 0.02 during a forward flight of 10 m/s, AOA of 5° and 2000 RPM [74, p. 37].

Comparing the hover data with the obtained results in Table 6.5, it can be seen I2 coincides closely with these findings. The same holds true for I3 and P3. However, M300's 0.010 deviates slightly from 0.013 as well as 1.95e-4 from 4.0e-5. Nevertheless, none of the results deviates considerably from each other. This similarity also applies to the values of c_D, which exhibit only small variations. Considering the diversity of data sources and the utilisation of different methods to calculate the parameters, it is reasonable to expect some uncertainty and a certain level of variability.

6.4 Validation of model

6.4.1 eCalc

The web-based calculator eCalc [81] is often used by companies [82] and multicopter enthusiasts in the estimation of drone performance, allowing its users to select a variety of components and adjust various parameters to calculate flight time and range. The calculator takes factors such as motor and propeller specifications into account, as well as battery capacity and voltage, model frame size and weight. Then users can determine the configuration for their specific needs.

By inserting the specifications for the M300 into the calculator, Figure 6.1a is given as a response. It can be observed flight time is decreasing steadily from hover at 0 m/s as the speed is increasing. This trend can be seen for both I3 and P3 as well in figures 6.1c and 6.1b. The available flight time for M300 does not fully match the numbers from DJI. Whereas the data sheets state a flight time of 55 minutes (at 7 m/s), 25 minutes (at 0 m/s), and 23 minutes (at 0 m/s) for M300, I3 and P3, eCalc states approximately 37 minutes, 23 minutes and 26 minutes, respectively.

Furthermore, when comparing the results from eCalc (Figure 6.1a, 6.1b, and 6.1c) with the simulations in Section 6.5, a notable difference is observed. The eCalc results show a consistent decrease in flight time as the speed increases, whereas the simulations demonstrate a slight increase in flight time before eventually decreasing as the speed increases. This may be an indication that an accurate model of inflow is not included in the eCalc calculations.

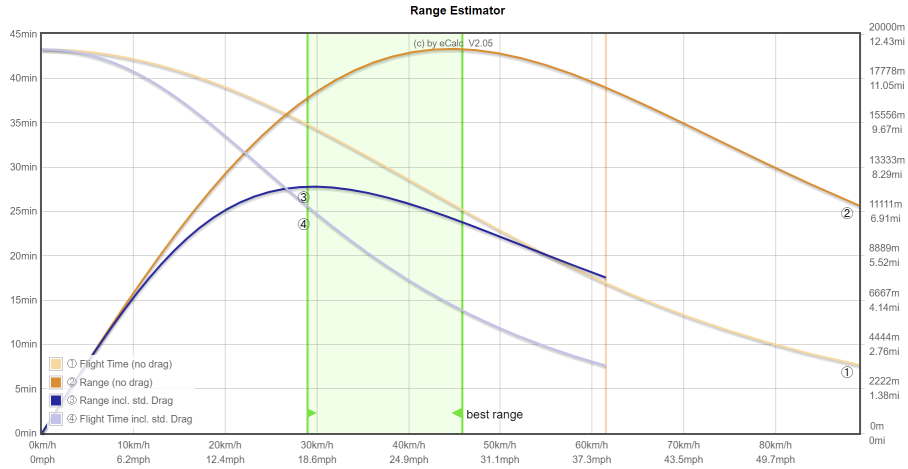

(a) eCalc results for M300

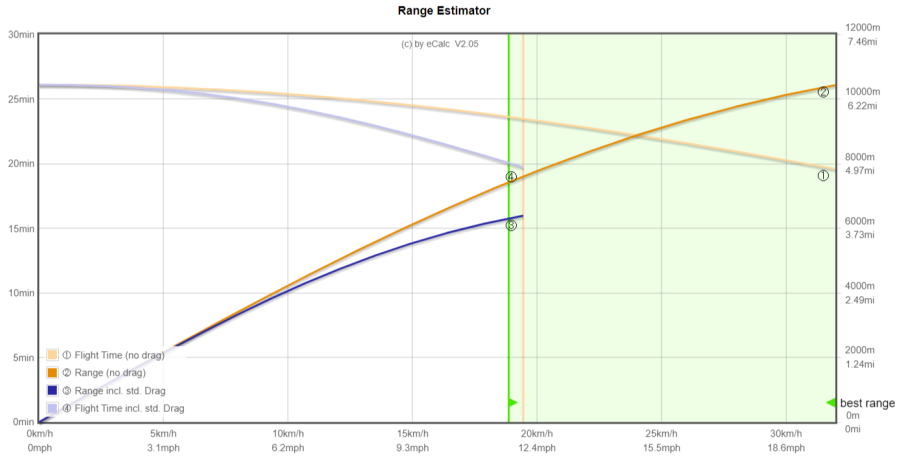

(b) eCalc results for P3

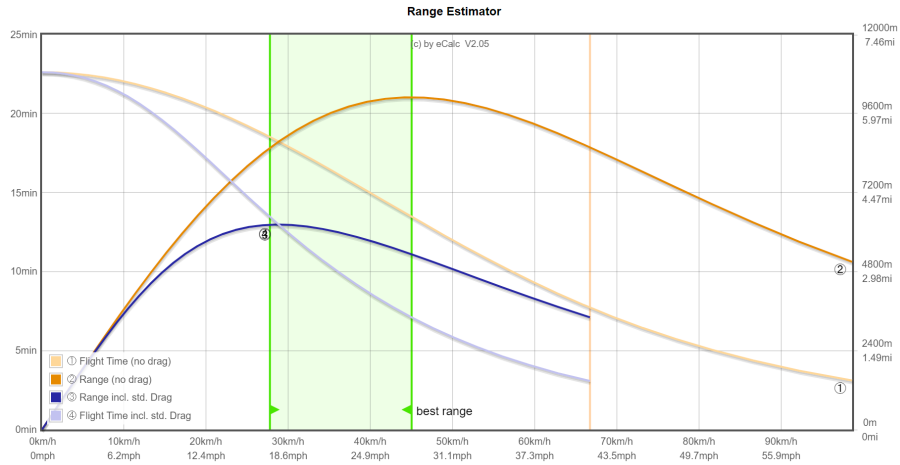

(c) eCalc results for I3

6.5 Simulated power consumption

For all simulations conducted, multirotors are modelled with evenly spaced rotors that are positioned at equal distances from each other on the same plane with non-overlapping rotors.

Furthermore, the rotor layout designates the rear rotor pair as rotors 1 and 2, while the front rotor pair comprises rotors 3 and 4. This is illustrated in Figure 6.2.

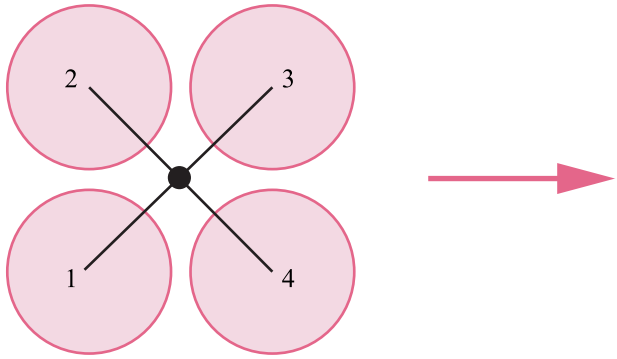

Figure 6.2: Rotor layout configuration where rotors 1 and 2 are situated at the rear, while rotors 3 and 4 are located at the front of the multirotor

6.5.1 M300

Figure 6.3a illustrates the distribution of power, parasitic, profile and induced. The findings presented in Figure 6.3b indicate that a speed of 7 m/s results in a flight time of 54 minutes, which aligns closely with the reported flight time of 55 minutes at the same speed as stated in the DJI data sheet. Moreover, hovering at 0 m/s results in 50 minutes of flight time, which can be attributed to the reduced induced drag that occurs when drones operate at lower speeds compared to hover.

According to Johnson [19, p. 34], the power loss distribution for a rotor in hover for helicopters is typically estimated to be approximately 60% induced power, 30% profile power, and 7-12% for other factors such as nonuniform inflow, wake swirl, and tip losses. However, the simulation results presented in Figure 6.3a do not align with these percentages. At 0 m/s, the profile power and induced power values are nearly equal, with values of 328 W and 326 W, respectively. This is closer to a 1:1 ratio rather than the 1:2 ratio.

As air flows through the front rotors of the drone, the energy extraction by these rotors and the disturbances created by the rotating blades interacting with the air can weaken and disrupt the smooth airflow. This disturbance results in the formation of a wake, leading to a significant reduction in power produced by the rear rotors compared to the front rotors. This trend is likely depicted in Figure 6.3c and Figure 6.3d, which display the induced power for each rotor. In the latter figure, it is likely that the rear rotor pair experiences wake losses. However, as the drone's forward speed increases to around 10-15 m/s, the amount of induced drag decreases. This is likely because the airflow around the rotors becomes more streamlined compared to hovering at 0 m/s. As a result, the drone can generate lift with greater efficiency, leading to a reduction in induced drag which can be seen as the bottom of the valley.

The optimisation analysis reveals that the optimal hovering speed for maximising flight time is determined to be 5.2 m/s, whereas the optimal speed for maximising distance is calculated to be 10.1 m/s These speeds correspond to flight times of 55 minutes and 44 minutes, or distances of 17.2 km and 26.7 km, respectively. These findings highlight the significance of selecting an appropriate flight speed in order to maximise the flight time and range capabilities of drones.

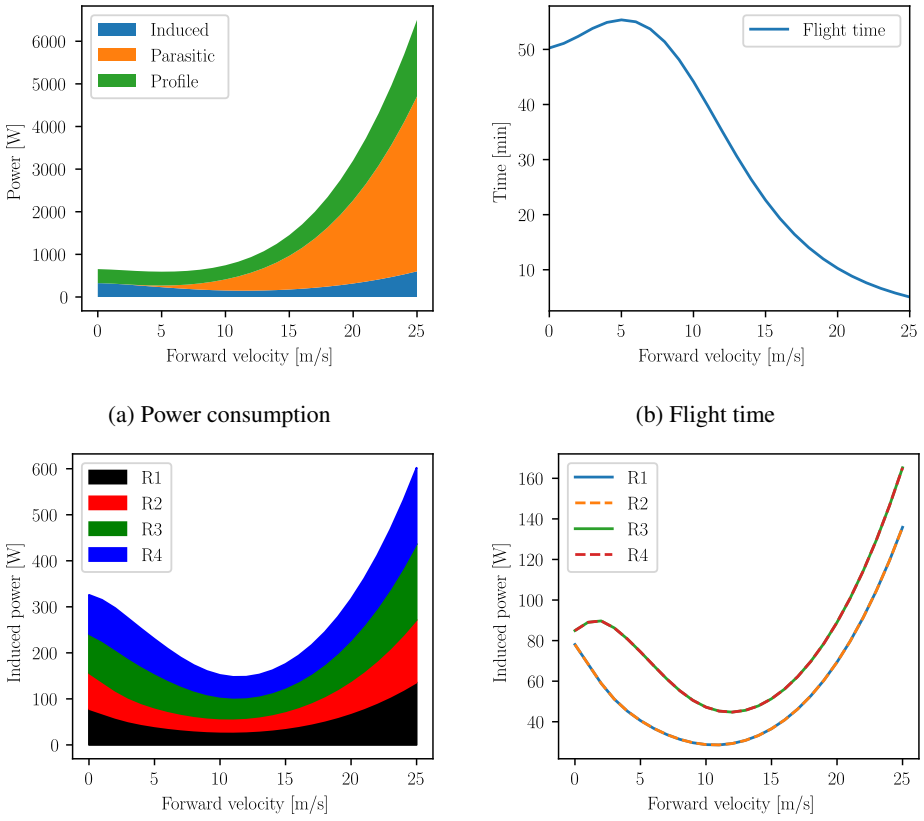

(a) Power consumption

(b) Flight time

(c) Induced power loss

(d) Induced power front and rear rotors

Figure 6.3: DJI data sheet simulation for M300

6.5.2 P3 NASA wind tunnel data

In Figure 6.4a, the power distribution is depicted. However, the hover power loss observed in the simulation does not align with Johnsen's power distribution, as the simulation results indicate a ratio of 1.3 between profile and induced power consumption during hover.

Specifically, profile power accounts for 88 W, while induced power amounts to 66 W. It is worth noting that the P3 drone has a relatively small size, with a vehicle frame measuring 350 mm in diagonal length, a weight of 1.27 kg, and propellers with a length of approximately 24 cm. As a result, it is reasonable to assume that the short and stubby wings of the P3 drone could contribute significantly to the total power loss.

Although RPM alone cannot provide a comprehensive assessment of a drone's performance, it is notable that the P3 drone has a high hover RPM of 5300 RPM. This indicates that the smaller drone's propulsion system operates at a relatively high rotational speed to sustain its position in the air. The elevated RPM requirement suggests that the P3 drone's propulsion system exerts greater effort to maintain stability during hovering, which in turn can contribute to a significant portion of the power consumption attributed to profile power.

In Figure 6.4b, the estimated flight time during hover is around 28 minutes, which closely aligns with the approximate value stated in the DJI data sheet of 25 minutes. The optimisation problem concludes the optimal speed for hovering at 0 m/s to be 6.6 m/s, resulting in a maximum estimated flight time of 32 minutes. Additionally, a speed of 13.3 m/s allows for achieving the longest possible distance, which corresponds to 24 minutes of flight time. This indicates a difference in reach of approximately 12.7 km compared to 19.2 km.

Furthermore, the figures representing induced power, namely Figure 6.4c and Figure 6.4d, demonstrate a similar wake effect as previously observed in the M300 drone. Specifically, the rear rotors exhibit lower power generation compared to the front rotors, indicating the presence of wake-induced losses.

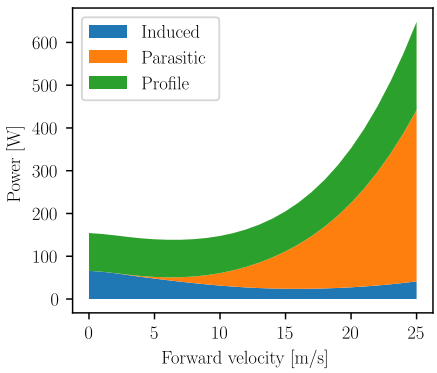

(a) Power consumption

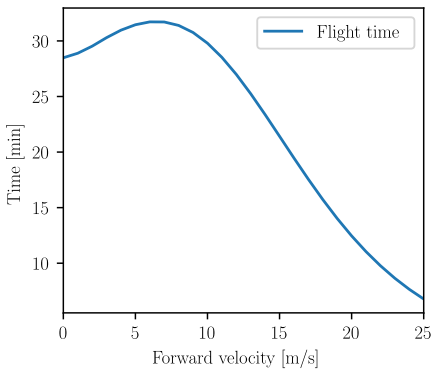

(b) Flight time

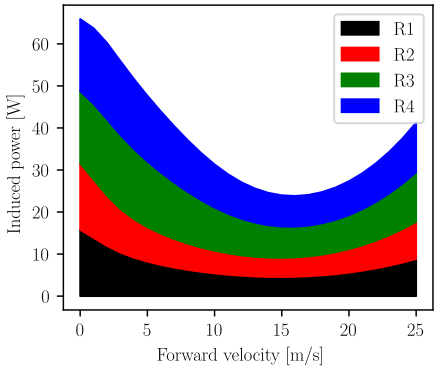

(c) Induced power

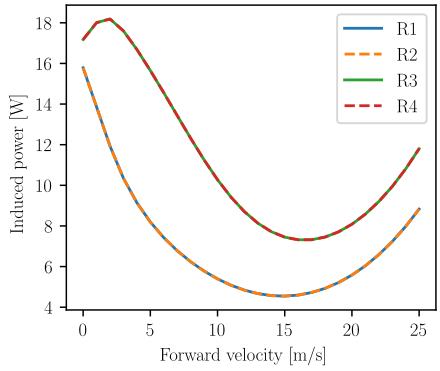

(d) Induced power front and rear rotors

Figure 6.4: NASA wind tunnel data simulation for P3

6.5.3 I3 data sheet

Figure 6.5 presents the simulation results for the I3 drone. However, the observed profile/induced power ratio of 1.2 deviates from Johnsen's approximations for helicopters [19, p. 34]. While it is acknowledged that multirotors and helicopters are not entirely identical, some similarities were still initially expected.

The results depicted in Figure 6.5a and Figure 6.5b indicate that hovering requires approximately 474 W of power, yielding an expected flight time of 25 minutes. These findings closely align with the specifications provided in the DJI data sheet, which also indicate a flight time of 25 minutes at a forward speed of 0 m/s.

Furthermore, the optimisation analysis reveals that the optimal speed for maximising flight time is determined to be 6.9 m/s, resulting in a flight time of 28 minutes. This differs from DJI's stated optimal hover speed of 10 m/s, which should also correspond to a flight time of 28 minutes. In range, this is a difference of 11.6 and 16.8 km. Additionally, the optimal range speed for the I3 drone is estimated to be 13.8 m/s which equals 21 minutes of flight time. The corresponding distance equals 17.4 km.

Similar to the previous results for M300 and P3, the graphs in Figure 6.5c and Figure 6.5d indicate that the rear pair of rotors generate less power compared to the front rotors. This observation further emphasises the presence of the wake effect, where the interaction of the front rotors with the air disrupts the flow and reduces the power output of the rear rotors.

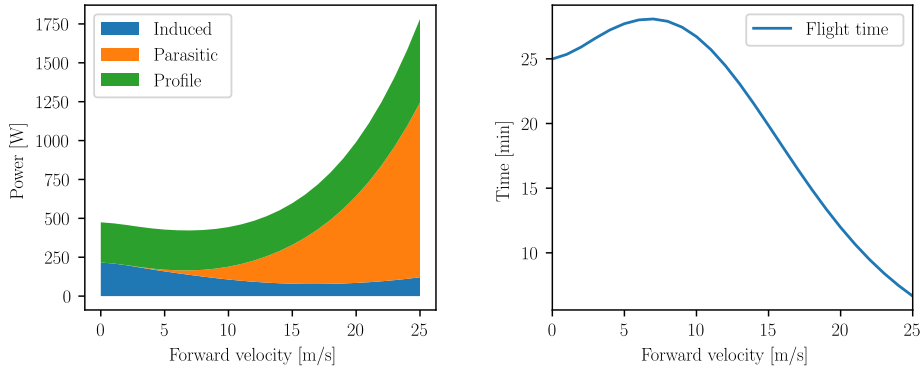

(a) Power consumption

(b) Flight time

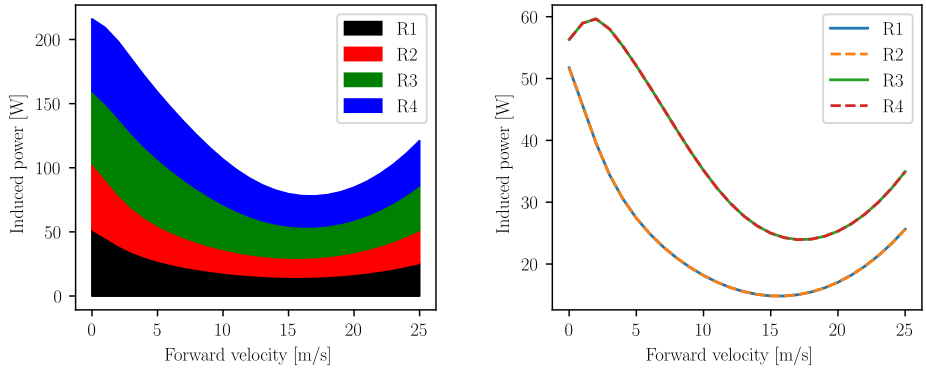

(c) Induced power loss

(d) Induced power front and rear rotors

Figure 6.5: DJI data sheet simulation for I3

6.5.4 I2 Xoar data

The laboratory test data for the I2 was used for comparison with the I3 due to the unavailability of one parameter for the I3, which had to be approximated. It should be noted that the efficiency constant for the I2 was measured as 0.72 [79], while for the I3, it was assumed to be 0.883. Additionally, the weight of the camera and lens is included in the I3 but excluded in the I2. However, considering that the I2 is almost seven years older than the I3, it is possible that significant improvements have been made to the drone during that time.

In the case of the I2, the power required at a forward velocity of 0 m/s was determined to be 415 W, with a flight time of 28 minutes. This is pictured in Figure 6.6a and 6.6b, and aligns well with the DJI data sheet's claim of 27 minutes including the lightest camera.

The optimal speed for max flight time for the I2 was estimated to be 6.9 m/s, resulting in a flight time of 31 minutes and a range of 12.1 km.

Additionally, the optimal distance speed for the I2 was estimated to be 13.8 m/s which corresponds to both 21 minutes of flight time and 17.4 km of distance. Despite using different data sources, the results for both the I3 and the I2 exhibit similarities. Overall, I2 does not deviate greatly from the results obtained for I3 in Subsection 6.5.3.

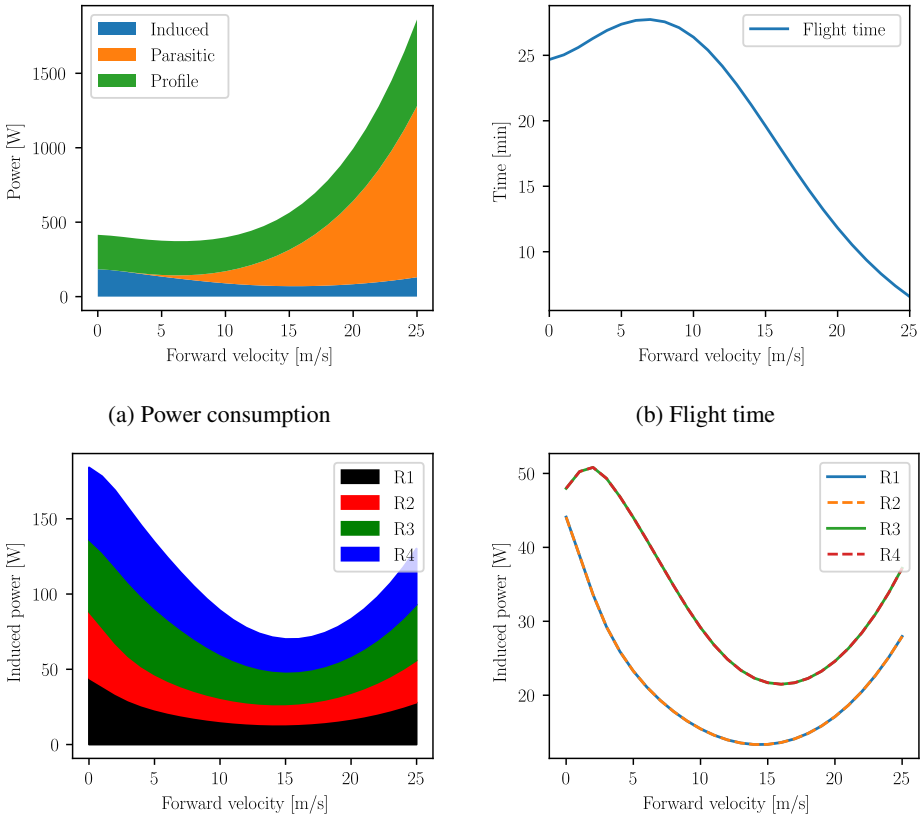

(a) Power consumption

(b) Flight time

(c) Induced power loss

(d) Induced power front and rear rotors

Figure 6.6: Test data simulation for I2

7 Results

Having established the reliability of the simulation framework in Chapter 6, the next step is to implement regulatory conditions as constraints into the optimisation problem. This allows for the simulation of case studies presented in Chapter 5 while ensuring compliance with applicable legislation. As a result, each section in Chapter 7 corresponds to the respective case sections presented in Chapter 5.

7.1 RO 3

For the case study regarding police drone use during larger events, a proposal was provided for defining conditions using RO 3 in Subsection 5.1.3 in chapter 5. These conditions were reformulated to align with equation (7.1), where the maximum horizontal speed $V_{\max}$ is determined to be 9.0 m/s.

$$0 \leq V_{\text{xi}} \leq V_{\max} = 9.0\,\text{m/s} \tag{7.1}$$

Incorporating this condition into the optimisation process yields the results shown in Figure 7.1a, revealing the optimal speeds for maximising flight time and range as 5.2 m/s and 9.0 m/s, respectively. This translates to flight times of approximately 55 minutes and 48 minutes, or distances of approximately 17.2 km and 25.9 km, respectively. As depicted in Figure 7.1b, the maximum flight time corresponds to the peak of the graph, while the maximum range slightly deviates from the peak to adhere to the specified regulations for this particular case.

Maximising airtime could be particularly advantageous for the police during larger events and monitoring operations. As events often span an extended duration, having the possibility of a longer airborne presence can be essential. The graphs shown in Figure 7.1b can probably be most useful on-site since it easily displays the consequence of increasing flight speed.

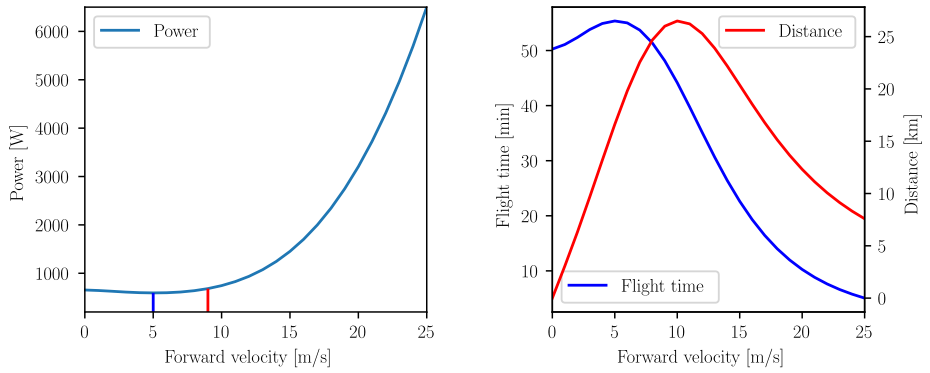

(a) Power consumption

(b) Flight time and range

Figure 7.1: DJI data sheet simulation for M300 with RO 3 regulatory constraints

7.2 RO 2

Within the context of the SAR mission case study, the result from optimising for the range is probably the most useful aspect. This is particularly important when dealing with extensive areas that require coverage and search efforts for missing individuals at sea. As previously mentioned, RO 2 imposes a maximum speed restriction of 80 knots, which can be expressed as shown in equation (7.2).

$$0 \leq V_{\text{xi}} \leq V_{\text{max}} = 80\,\text{knots} \tag{7.2}$$

The simulation results are presented in Figure 7.2a. The figure demonstrates that the regulatory constraints do not have an impact on the optimal speeds for achieving maximum flight time or maximum range, as it shows the exact identical result from the previous chapter in Subsection 6.5.1. Consequently, a speed of 10.1 m/s is determined as the optimal choice for covering the maximum possible distance during forward flight. This can be crucial if a person is missing, and it is urgent to have as much sea area as possible investigated.

However, it is important to consider the experience and training of the drone pilot in charge during the mission. For an untrained individual who relies solely on visual cues displayed on the screen of a smart controller, a speed of 10.1 m/s may be too fast when attempting to locate a missing person in the sea. In such cases, Figure 7.2b could for instance provide valuable insights for determining an alternative speed suitable for beginners.

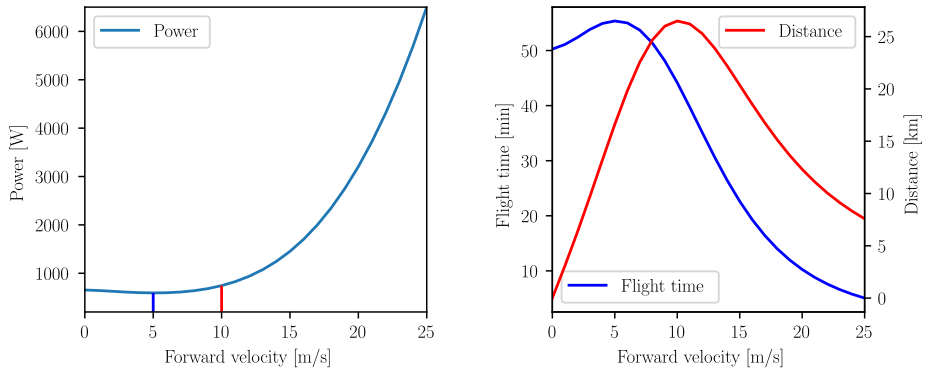

(a) Power consumption

(b) Flight time and range

Figure 7.2: DJI data sheet simulation for M300 with RO 2 regulatory constraints

7.3 PDRA-G03

Performing linear inspections using PDRA-G03 involves a well-defined type of operation, where the maximum forward flight is limited by the specified height and ground risk buffer. As described in Subsection 5.3.3 in Chapter 5, this entails maintaining a maximum height of 30 m above the pole height for obstacles up to 20 m in height, and a maximum height of 15 m above the pole height for obstacles taller than 20 m. The simulation results indicate that regulatory conditions do not impact the optimal speeds, and is shown in Table 7.1. This is most likely to the default criteria of the 1:1 rule.

As previously stated in Subsection 6.5.1 in Chapter 6, 5.2 m/s and 10.1 m/s equals 55 minutes and 44 minutes, or distances of 17.2 km and 26.7 km, respectively. Consequently, the difference is 9.5 km of high-voltage lines, which could be more dependent on the forward speed chosen. This is the same result as for the previous case, shown in Figure 7.2b.

However, it should be noted that ensuring an adequate ground risk buffer according to the 1:1 rule can be challenging in certain scenarios. Nevertheless, for the purpose of this example, it is assumed to be achievable since the case was written with sparsely populated areas in mind. Another note is that the battery is assumed to be used 100%, which is not recommended for the battery health, and therefore all distances will realistically be lower. Nevertheless, that would apply to all speeds.

Table 7.1: M300 and PDRA-G03

Pole height $\leq$ 20 m	**Max height AGL**	**Maximum flight time**	**Maximum range**
9 m	39 m	5.2 m/s	10.1 m/s
19 m	49 m	5.2 m/s	10.1 m/s
Pole height $>$ 20 m	**Max height AGL**	**Maximum flight time**	**Maximum range**
25 m	40 m	5.2 m/s	10.1 m/s
39 m	53 m	5.2 m/s	10.1 m/s

7.4 SORA

Filming in close proximity to crowds poses greater risks in the event of a sudden drone failure and subsequent fall. However, imposing excessively strict limitations on flight proximity can hinder the effective capture of the desired subject. Therefore, it is important to strike a balance between safety and capturing optimal results in photography and cinematography by maintaining a closer proximity to the subject. Unlike the previous case where a 1:1 rule was applied, alternative proximity constraints are utilised in this scenario, which influence the optimisation process as shown in Table 7.2.

Table 7.2: I3 and specific SORA

	Heights (m) AGL			
	25	50	80	120
50 m proximity				
Maximum horizontal speed (m/s)	15	9.5	6.5	4.5
Maximum flight time (m/s)	6.9	6.9	6.5	4.5
Maximum range (m/s)	13.8	9.5	6.5	4.5
25 m proximity				
Maximum horizontal speed (m/s)	7.5	4.5	3	2.5
Maximum flight time (m/s)	6.9	4.5	3	2.5
Maximum range (m/s)	7.5	4.5	3	2.5

Figure 7.3 shows a simulation that incorporates a maximum horizontal speed of 15 m/s as a constraint. As shown in Table 7.2, optimising with this regulatory constraint yield the same result as when no constraints are applied. Moreover, the graphs presented in Figure 7.3b provide a reliable and visual basis for estimating and selecting appropriate flying speeds for the I3, which can be highly beneficial during filming operations on location.

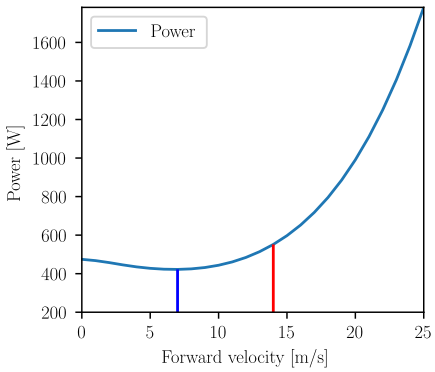

(a) Power consumption with maximum horizontal speed 15 m/s

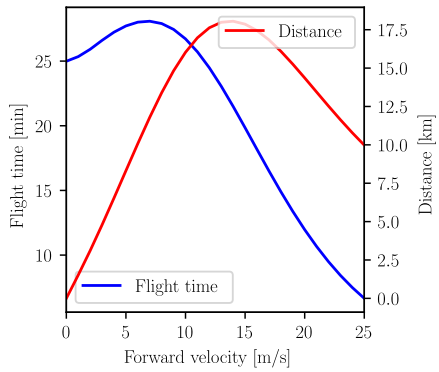

(b) Flight time and range

Figure 7.3: DJI data sheet simulation for I3 with regulatory constraints

8 Conclusion

Multiple case studies have been identified and described, highlighting the potential operational benefits of minimising power losses. In addition to the constructed case studies in Chapter 5, the use of the simulation framework has the potential to be extended in various other domains, such as drone package delivery or conducting inspections of railways or agriculture. Therefore, the application of usage can be far wider than demonstrated so far.

The adoption of a scalable simulation framework in these studies offers an effective means to determine optimal forward speeds for various drone applications, providing noteworthy benefits to drone operators. As results show, adjustments in flying strategies can greatly contribute to maximising flight time and expanding range coverage. It is essential to recognise the significance of efficiently utilising available resources.

Furthermore, optimising compliance with current laws and regulations is an important aspect. The rapid increase of UAVs necessitates effective regulation to ensure the safety of operations and to address potential risks. Therefore, optimising within the boundaries of current regulations is a crucial aspect. By aligning optimisation strategies with regulatory requirements, drone operators can strike a balance between maximising performance and adhering to legal frameworks, thus promoting safe and responsible drone usage.

Moreover, considerable time and effort have been dedicated to calculating and determining the parameters for the simulation model, taking into account the available data available. The accuracy of these parameters has been confirmed through a comparison with existing numbers derived from real-world tests, demonstrating a close alignment with the findings of Nguyen et al. [74].

Consequently, it can be concluded the simulation model provides reasonable and valid answers for all the given simulation examples, regardless of whether the data source originated from a wind tunnel, data sheet, or laboratory experiment. The model has also briefly been compared to the eCalc calculator. Although the plots did yield different estimates of available flight time and range for the M300, they were not too far off for the other drones, P3 and I3.

8.1 Future work

8.1.1 Collecting more data from real-world tests

Although the simulation results aligned well with the numbers provided in the data sheets, it would be beneficial to conduct additional real-world tests on physical multirotors. This would help ascertain whether any discrepancies exist between theoretical estimations and actual performance. Real-world testing could possibly provide valuable insights into the practical behaviour of multirotor systems and can potentially contribute to the further validation and refinement of the simulation framework, despite the already promising results obtained.

Some time was dedicated to conducting two tests in late May, which were successfully completed. However, due to the limited time available at that point, it was not possible to thoroughly examine and analyse the data in a satisfactory manner or proceed with further data processing. Nevertheless, upon initial inspection, the data appears to be promising, as a notable difference between rear and front rotors is observed.

Figure 8.2 is included to display one of the runs of the collected raw data. The motor speed for the rear rotors is represented by the blue and purple lines, while the front rotors are indicated by the red and green lines. Further exploration of the data would be highly interesting, as well as simulating the drone that collected the data using the simulation framework for comparison. Such an analysis could potentially contribute to a more comprehensive validation of the model.

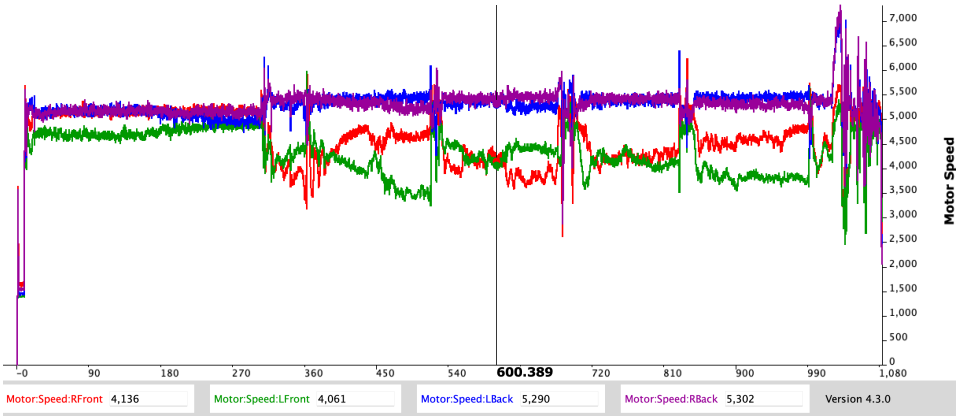

(a) Motor RPM

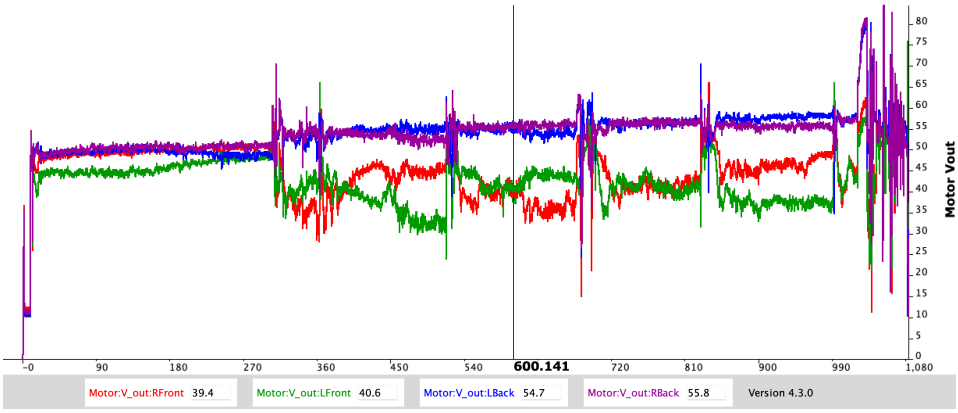

(a) Motor volt

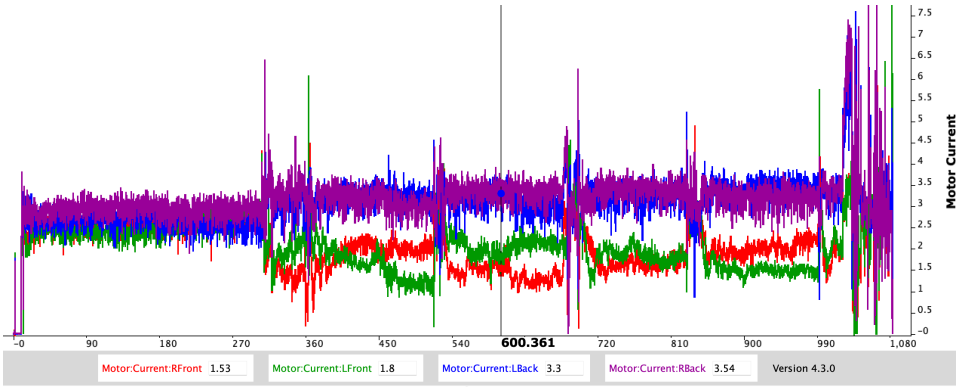

(b) Motor current

Figure 8.2: First test

8.1.2 Further implementation of regulations for UAVs

The drones selected for the presented case studies are relatively small compared to the size and weight permitted in specific categories and potentially certified. However, since EASA's regulatory framework is still being developed and essential materials have not yet been released, this aspect was not within the focus scope. Nevertheless, for future work, it would be interesting to explore case studies associated with higher risks.

The results demonstrate that optimising energy consumption for smaller UAVs yields minutes of increased flight duration. However, for larger drones with more available energy, modifying the speed can possibly have a more substantial effect. It would be both interesting and insightful to conduct similar simulations in the future when, for instance, drone taxis are ready to enter the air space.

8.1.3 Selection of case studies and multirotors

While four specific case studies were chosen for analysis, there are undoubtedly other cases that could be explored. In these particular studies, quadcopters were selected as they are commonly employed in various applications today. However, it is important to note that other rotor configurations exist and are utilised across different industries. For instance, octocopters, such as the Freefly's Alta series, are currently employed in aerial cinematography due to their ability to carry heavier film cameras. These alternative configurations offer unique advantages and may be worth investigating in future research.

Bibliography

[1] Finn Matras and Morten Dinhoff Pedersen. Multirotor inflow dynamics. *American Institute of Aeronautics and Astronautics (AIAA) Journal*, 2023, submitted.

[2] Thor Inge Fossen. *Handbook of Marine Craft Hydrodynamics and Motion Control*. Wiley, 2021.

[3] DJI. Phantom 1 specs, 2013. Accessed: 14.02.2023 https://www.dji.com/no/phantom/info.

[4] Expert drones. 3dr iris+, 2021. Accessed: 26.02.2023 https://www.expertdrones.com/alldrones/3dr-iris-915-mhz.

[5] Quadcopter. Freefly cinestar, 2023. Accessed: 26.02.2023 https://shop.quadrocopter.com/Freefly-CineStar_ep_63-1.html.

[6] Lovdata. Forskrift om luftfartøy som ikke har fører om bord (bsl a 7-1), 2016. Updated: 01.01.2021. Accessed: 16.01.2023 https://lovdata.no/forskrift/2015-11-30-1404.

[7] Lovdata. Forskrift om luftfart med ubemannet luftfartøy i åpen- og i spesifikk kategori (bsl a 7-2), 2021. Updated: 11.12.2022. Accessed: 16.01.2023 https://lovdata.no/forskrift/2020-11-25-2460.

[8] European Union Aviation Safety Agency. Certified category - civil drones, 2023. Accessed: 09.02.2023 https://www.easa.europa.eu/en/domains/civil-drones/drones-regulatory-framework-background/certified-category-civil-drones.

[9] DJI Oslo. Matrice 300 rtk, 2023. Accessed: 27.02.2023 https://djioslo.no/produkt/matrice-300-rtk/dji-matrice-300-rtk/.

[10] DJI. Inspire 3, 2023. Updated: 13.04.2023. Accessed: 13.04.2023 https://www.dji.com/no/inspire-3.

[11] Yacef Fouad, Nassim Rizoug, Omar Bouhali, and Mustapha Hamerlain. Optimization of energy consumption for quadrotor uav. *International Micro Air Vehicle Conference and Flight Competition (IMAV)*, 2017. Accessed: 14.05.2023 https://www.researchgate.net/publication/321161643_Optimization_of_Energy_Consumption_for_Quadrotor_UAV.

[12] Daniel Gandolfo, Lucio Salinas, Alexandre Santos Brandão, and Juan Toibero. Stable path-following control for a quadrotor helicopter considering energy consumption. *IEEE Transactions on Control Systems Technology*, 2016. Accessed: 14.05.2023 https://doi.org/10.1109/TCST.2016.2601288.

[13] Finn Matras. *Multiaspect power optimization based on induced flow considerations*. Norwegian University of Science and Technology, 2020.

[14] Rens Werink. On the control allocation of fully-actuated and over-actuated multirotor uavs, 2019. Accessed: 25.01.2023 https://www.semanticscholar.org/paper/On-the-control-allocation-of-fully-actuated-and-Werink/7e039f1bdf52d24dabee066cbe2a8330874aa4f2.

[15] James Rennie. Drone types: Multi-rotor, fixed-wing, single rotor, hybrid vtol - auav. *AUAV*, 2016. Accessed: 27.01.2023 https://www.auav.com.au/articles/drone-types/#1.

[16] Federal Aviation Administration. Helicopter flying handbook, 2019. Updated: 29.03.2022. Accessed: 12.05.2023 https://www.faa.gov/regulations_policies/handbooks_manuals/aviation/helicopter_flying_handbook.

[17] Federal Aviation Administration. Pilot's handbook of aeronautical knowledge, 2016. Accessed: 30.01.2023 https://www.faa.gov/regulations_policies/handbooks_manuals/aviation/phak.

[18] James E. Vance and Walter James Boyne. Airplane, 2021. Accessed: 30.01.2023 https://www.britannica.com/technology/airplane.

[19] Wayne Johnson. Helicopter theory, 1994. Accessed: 06.02.2023 https://books.google.cv/books?id=SgZheyNeXJIC.

[20] Amila Thibbotuwawa, Peter Nielsen, Zbigniew Banaszak, and Grzegorz Bocewicz. Energy consumption in unmanned aerial vehicles: A review of energy consumption models and their relation to the uav routing: Part ii, 2019. Accessed: 02.02.2023 https://doi.org/10.1007/978-3-319-99996-8_16.

[21] International Civil Aviation Organization. About icao, 2022. Accessed: 03.02.2023 https://www.icao.int/about-icao/Pages/default.aspx.

[22] European Union Aviation Safety Agency. The agency, 2023. Accessed: 03.02.2023 https://www.easa.europa.eu/en/the-agency/the-agency.

[23] European Union Aviation Safety Agency. Easa by country, 2023. Accessed: 03.02.2023 https://www.easa.europa.eu/en/domains/international-cooperation/easa-by-country.

[24] Regjeringen. Forordning om u-space, 2017. Updated: 06.01.2023. Accessed: 18.01.2023 https://www.regjeringen.no/no/sub/eos-notatbasen/notatene/2017/aug/u-space/id2570869/.

[25] CAA Norway. What we do, 2023. Accessed: 03.02.2023 https://luftfartstilsynet.no/en/.

[26] CAA Norway. Engelsk mal for operasjonsmanual, 2022. Accessed: 09.02.2023 https://luftfartstilsynet.no/globalassets/dokumenter/dronedokumenter/nytt-eu-regelverk/operations-manual-template---amc.pdf.

[27] CAA Norway. Åpen kategori, 2022. Accessed: 09.02.2023 https://luftfartstilsynet.no/droner/apen-kategori/.

[28] CAA Norway. Slik søker du om tillatelse basert på sora, 2022. Accessed: 09.02.2023 https://luftfartstilsynet.no/droner/soke-om-tillatelse-i-spesifikk-kategori/soke-om-tillatelse2/.

[29] Eirik Helland Urke. Norsk drone sniffer seg fram til svolvelsyndere i middelhavet. *Teknisk Ukeblad*, 2021. Updated: 22.09.2021. Accessed: 09.02.2023 https://www.icao.int/about-icao/Pages/default.aspx.

[30] DJI. High-precision plant stand count for corn, sunflower and sugar beet by a drone and ai. *DJI Agriculture*, 2022. Updated: 08.10.2022. Accessed: 09.02.2023 https://ag.dji.com/case-studies/ag-news-en-precision-farming-2022.

[31] CAA Norway. Sertifisert kategori, 2022. Accessed: 09.02.2023
https://luftfartstilsynet.no/droner/veiledning/sertifisert-kategori/.

[32] European Union Aviation Safety Agency. Easy access rules for unmanned aircraft systems (regulation (eu) 2019/947 and regulation (eu) 2019/945), 2022. Updated: 22.09.2022. Accessed: 28.02.2023
https://www.easa.europa.eu/en/downloads/110913/en.

[33] Lukáš Bláha, Ondřej Severa, Martin Goubej, Tomáš Myslivec, and Jan Reitinger. Automated drone battery management system. *Drones*, 7(4), 2023. Accessed: 14.05.2023
https://www.mdpi.com/2504-446X/7/4/234.

[34] Tadeusz Czachórski, Erol Gelenbe, Godlove Suila Kuaban, and Dariusz Marek. Optimizing energy usage for an electric drone. *Springer International Publishing*, 2022. Accessed: 15.05.2023
https://doi.org/10.1007/978-3-031-09357-9_6.

[35] Chase C. Murray and Amanda G. Chu. The flying sidekick traveling salesman problem: Optimization of drone-assisted parcel delivery. *Transportation Research Part C: Emerging Technologies*, 2015. Accessed: 15.05.2023
https://www.sciencedirect.com/science/article/pii/S0968090X15000844.

[36] Yisak Debele, Ha-Young Shi, Assefinew Wondosen, Jin-Hee Kim, and Beom-Soo Kang. Multirotor unmanned aerial vehicle configuration optimization approach for development of actuator fault-tolerant structure. *Special Issue Unmanned Aerial Vehicles*, 2022. Accessed: 13.02.2023
https://doi.org/10.3390/app12136781.

[37] W.E. Baker, P.A. Cox, J.J. Kulesz, R.A. Strehlow, and P.S. Westine. *Explosion Hazards and Evaluation*. Elsevier Science B.V., 1983.

[38] Zoran Benić, Petar Piljek, and Denis Kotarski. Mathematical modelling of unmanned aerial vehicles with four rotors. *Interdisciplinary Description of Complex Systems*, 14:88–100, 01 2016. Accessed: 17.02.2023
https://www.researchgate.net/publication/292176923_Mathematical_Modelling_of_Unmanned_Aerial_Vehicles_with_Four_Rotors.

[39] E.M. Greitzer, Z.S. Spakovszky, and I.A. Waitz. Thermodynamics and propulsion, 2008. Accessed: 12.02.2023
https://web.mit.edu/16.unified/www/FALL/thermodynamics/notes/notes.html.

[40] J. Gordon Leishman. *Principles of helicopter aerodynamics*. Cambridge University Press, 2006.

[41] Jeff Bezanson, Alan Edelman, Stefan Karpinski, and Viral B Shah. Julia: A fresh approach to numerical computing. *SIAM review*, 59(1):65–98, 2017. Accessed: 26.05.2023
https://doi.org/10.1137/141000671.

[42] Miles Lubin, Oscar Dowson, Joaquim Dias Garcia, Joey Huchette, Benoît Legat, and Juan Pablo Vielma. Jump 1.0: Recent improvements to a modeling language for mathematical optimization. *Mathematical Programming Computation*, 2023. In press.

[43] Andreas Wächter and Lorenz T. Biegler. On the implementation of an interior-point filter line-search algorithm for large-scale nonlinear programming. *Mathematical Programming*, 106:25–57, 2006.

[44] JuMP. Jump documentation, 2023. Accessed: 26.05.2023
https://jump.dev/.

[45] Ipopt documentation. Ipopt documentation, 2023. Accessed: 26.05.2023
https://coin-or.github.io/Ipopt/index.html.

[46] Asia Perspective. China's thriving drone industry, 2021. Accessed: 26.02.2023
https://www.asiaperspective.com/china-thriving-drone-industry/.

[47] European Union Aviation Safety Agency. Amc and gm to implementing regulation (eu) 2021/664 — issue 1, 2022. Accessed: 18.01.2023
https://www.easa.europa.eu/en/document-library/acceptable-means-of-compliance-and-guidance-materials/amc-and-gm-implementing.

[48] Cristina Barrado, Mario Boyero, Luigi Brucculeri, Giancarlo Ferrara, Andrew Hately, Peter Hullah, David Martin Marrero, Enric Pastor, Anthony Rushton, and Andreas Volkert. U-space concept of operations: A key enabler for opening airspace to emerging low-altitude operations. *Aerospace*, 7:24, 03 2020. Accessed: 07.02.2023
https://doi.org/10.3390/aerospace7030024.

[49] Regjeringen. Implementeringsforordning om luftfartsoperasjoner med ubemannede luftfartøyer, 2017. Updated: 17.11.2022. Accessed: 14.02.2023 https://www.regjeringen.no/no/sub/eos-notatbasen/notatene/2015/sep/a-npa-2015-regelverk-om-dronerrpas/id2458752/.

[50] CAA Norway. Regulations of drones, 2021. Accessed: 17.01.2023 https://luftfartstilsynet.no/en/drones/commercial-use-of-drones/about-dronesrpas/regulations-of-drones/.

[51] European Union Aviation Safety Agency. Specific category - civil drones, 2023. Accessed: 28.02.2023 https://www.easa.europa.eu/en/domains/civil-drones-rpas/specific-category-civil-drones.

[52] CAA Norway. Spesifikk kategori, 2022. Accessed: 28.02.2023 https://luftfartstilsynet.no/droner/spesifikk-kategori/.

[53] CAA Norway. Sora – specific operation risk assessment, 2022. Accessed: 27.03.2023 https://luftfartstilsynet.no/droner/sora---specific-operation-risk-assessment/.

[54] European Union Aviation Safety Agency. Specific operations risk assessment (sora), 2023. Accessed: 28.02.2023 https://www.easa.europa.eu/en/domains/civil-drones-rpas/specific-category-civil-drones/specific-operations-risk-assessment-sora.

[55] European Union Aviation Safety Agency. Predefined risk assessment (pdra), 2023. Accessed: 26.02.2023 https://www.easa.europa.eu/en/domains/civil-drones-rpas/specific-category-civil-drones/predefined-risk-assessment-pdra.

[56] CAA Norway. Slik søker du om tillatelse for å fly etter en pdra, 2022. Accessed: 28.02.2023 https://luftfartstilsynet.no/droner/soke-om-tillatelse-i-spesifikk-kategori/soke-om-tillatelse-til-pdra/.

[57] CAA Norway. Regler for sivil statsluftfart med drone, 2021. Accessed: 23.01.2023 https://luftfartstilsynet.no/aktorer/regelverk/aic/aic-n/2021/3021-regler-for-sivil-statsluftfart-med-drone/.

[58] Vilde Bratland Hansen. Usa frykter spionasje og skroter kinesiske droner. i norge skal politiet kjøpe 130. *Aftenposten*, 2022. Accessed: 27.02.2023 https://www.aftenposten.no/verden/i/Kzqp2M/usa-frykter-spionasje-og-skroter-kinesiske-droner-i-norge-skal-politiet-kjoepe-130.

[59] Hans O. Torgersen. Slik kan politiets drone se deg fra luften. *Aftenposten*, 2020. Updated: 21.06.2020. Accessed: 04.03.2023 https://www.aftenposten.no/norge/i/Vb0mB1/slik-kan-politiets-drone-se-deg-fra-luften.

[60] Aurora Berg. Politiet skal overvåke rakettnatt med droner. – kan skape usikkerhet, mener datatilsynet. *NRK*, 2022. Updated: 26.08.2022. Accessed: 04.03.2023 https://www.nrk.no/tromsogfinnmark/politiet-bruker-droner-pa-festivaler_-men-datatilsynet-mener-det-bryter-personvernet-1.16080037.

[61] Erik Inderhaug. Hobbybutikk fra grimstad skal levere droner til politiet. *Politiforum*, 2021. Updated: 17.12.2021. Accessed: 21.03.2023 https://www.politiforum.no/droner-jorgen-lunde-ronge/hobbybutikk-fra-grimstad-skal-levere-droner-til-politiet/221360.

[62] Martin Næss Kristiansen. Brannslokkere blir dronepiloter: – kan redde liv og begrense skader. *Dagsavisen*, 2013. Updated: 27.01.2023. Accessed: 28.03.2023 https://www.dagsavisen.no/demokraten/nyheter/2023/01/27/brannslokkere-blir-dronepiloter-kan-redde-liv-og-begrense-skader/.

[63] Follo Brannvesen IKS. Droneberedskap, 2013. Updated: 24.03.2023. Accessed: 28.03.2023 https://www.follobrannvesen.no/dronetjeneste.569783.no.html.

[64] DJI. Matrice 300 rtk, 2023. Accessed: 27.02.2023 https://www.dji.com/no/matrice-300/downloads.

[65] DJI. Matrice 300 rtk - user manual v3.2, 2022. Updated: 18.10.2022. Accessed: 27.02.2023 https://dl.djicdn.com/downloads/matrice-300/20221018/M300_RTK_User_Manual_EN_v3.2%201018.pdf.

[66] DJI. Matrice 300 rtk - 2110 propeller product information, 2022. Updated: 17.06.2020. Accessed: 27.02.2023
https://dl.djicdn.com/downloads/matrice-300/20200617/2110_Propeller_Product_Information.pdf.

[67] Lovdata. Forskrift om lufttrafikkregler (bsl f 1-1)), 2093. Updated: 11.03.2003. Accessed: 01.03.2023
https://lovdata.no/dokument/LTI/forskrift/2003-02-07-252.

[68] eCalc. Hovedredningssentralen, 2023. Accessed: 08.05.2023
https://www.hovedredningssentralen.no/english/.

[69] International Aeronautical, Maritime Search, and Rescue Manual. Iamsar manual volume ii mission co-ordination, 2016. Accessed: 01.05.2023
http://www.icscc.org.cn/upload/file/20190102/Doc.9731-EN%20IAMSAR%20Manual%20-%20International%20Aeronautical%20and%20Maritime%20Search%20and%20Rescue%20Manual%20Volume%20II%20-%20Mission%20Co-ordination.pdf.

[70] Luis Luque-Vega, Bernardino Castillo-Toledo, Alexander Loukianov, and Luis González-Jiménez. Power line inspection via an unmanned aerial system based on the quadrotor helicopter. *Proceedings of the Mediterranean Electrotechnical Conference - MELECON*, 2014. Accessed: 12.03.2023
https://www.researchgate.net/publication/271453876_Power_line_inspection_via_an_unmanned_aerial_system_based_on_the_quadrotor_helicopter.

[71] NASA. Terminal velocity interactive, 2022. Updated: 19.08.2022. Accessed: 13.03.2023
https://www1.grc.nasa.gov/beginners-guide-to-aeronautics/termvel/#terminal-velocity.

[72] Andrew V. Shelley. Ground risk for large multirotor uavs, 2021. Updated: 29.01.2022. Accessed: 10.03.2023
https://www.academia.edu/53282063/Ground_Risk_Buffer_for_Large_Multirotor_UAVs.

[73] Andrew Shelley. A model of human harm from a falling unmanned aircraft: Implications for uas regulation. *International Journal of Aviation, Aeronautics, and Aerospace*, 2016. Accessed: 12.03.2023
https://doi.org/10.15394/ijaaa.2016.1120.

[74] Duc Nguyen, Yu LIU, and Koichi Mori. Experimental study for aerodynamic performance of quadrotor helicopter. *TRANSACTIONS OF THE JAPAN SOCIETY FOR AERONAUTICAL AND SPACE SCIENCES*, pages 29–39, 01 2018. Accessed: 23.02.2023
https://www.researchgate.net/publication/322241145_Experimental_Study_for_Aerodynamic_Performance_of_Quadrotor_Helicopter.

[75] Mitsuhide Sato, Masami Nirei, Yuichiro Yamanaka, Tatsuki Suzuki, Yinggang Bu, and Tsutomu Mizuno. Increasing the efficiency of a drone motor by arranging magnetic sheets to windings. *Energy Reports*, 6:439–446, 2020. Accessed: 24.04.2023
https://www.sciencedirect.com/science/article/pii/S2352484719309199.

[76] Mejzlik Propellers. Propulsion system data, 2023. Accessed: 24.04.2023
https://www.mejzlik.eu/technical-data/propulsion_system_data.

[77] Carl Russell, Gina Willink, Colin Theodore, Jaewoo Jung, and Brett Glasner. Wind tunnel and hover performance test results for multicopter uas vehicles, 2018. Accessed: 09.04.2023
https://rotorcraft.arc.nasa.gov/Publications/files/Russell_1180_Final_TM_022218.pdf.

[78] DJI. Phantom 3 specs, 2017. Accessed: 09.04.2023
https://www.dji.com/no/phantom-3-standard.

[79] Xoar Propellers. Pjp-t-l-in2, 2023. Accessed: 26.04.2023
https://www.xoarintl.com/multicopter-propellers/photography-drone-props/PJP-T-L-1550-INS-dji-inspire-2-carbon-fiber-propellers/.

[80] DJI. Inspire 2, 2017. Accessed: 28.02.2023
https://www.dji.com/no/inspire-2.

[81] eCalc. Multicopter calculator, 2022. Updated: 17.6.2022. Accessed: 13.03.2023
https://ecalc.ch/xcoptercalc.php.

[82] eCalc. Multicopter partner, 2023. Accessed: 19.05.2023
https://www.ecalc.ch/partner.htm.

NTNU

Norwegian University of
Science and Technology